

1 **Impact of Vertical Resolution on Representing Baroclinic Modes and Water Mass**

2 **Distribution in the North Atlantic**

3 Xiaobiao Xu, Eric P. Chassignet, and Alan J. Wallcraft

4 Center for Ocean-Atmospheric Prediction Studies, Florida State University

5

6 A manuscript submitted to *Ocean Modelling*

7

8

9 **Abstract**

10 In contrast to the large volume of studies on the impact of horizontal resolution in oceanic general  
11 circulation models (OGCMs), the impact of vertical resolution has been largely overlooked and  
12 there is no consensus on how one should construct the vertical grid to represent the vertical  
13 structure of the baroclinic modes as well as the distribution of distinct water masses throughout  
14 the global ocean. In this paper, we document the importance of vertical resolution in the  
15 representations of vertical modes and water masses in the North Atlantic and show i) that vertical  
16 resolution is unlikely to undermine the resolution capability of the horizontal grid in representing  
17 the vertical modes and a 32-layer isopycnal configuration is adequate to represent the first five  
18 baroclinic modes in mid-latitudes and ii) that vertical resolution should focus on representing water  
19 masses. A coarse vertical resolution (16-layer) simulation exhibits virtually no transport in the  
20 dense overflow water which leads to a weaker and significantly shallower Atlantic meridional  
21 overturning circulation (AMOC) despite resolving the first baroclinic mode throughout the domain,  
22 whereas there are overall very small differences in the subtropical and subpolar North Atlantic  
23 circulation in the simulations with finer vertical resolution (24 to 96 layers). We argue that  
24 accurately representing the water masses is more important than representing the baroclinic modes  
25 for an OGCM in modeling the low-frequency large-scale circulation.

## 26 **1. Introduction**

27 Oceanic general circulation models (OGCMs), with the underlying algorithmic formulation  
28 principles first proposed by Bryan (1969) in the 1960s (McWilliams 1996), have become an  
29 essential supplement to the more traditional methodologies in physical oceanography, i.e., theory  
30 and observations, and have a wide range of applications (e.g., Le Sommer et al., 2018). They are  
31 used to test hypotheses for mechanisms underlying oceanic observations in idealized or realistic  
32 configurations, to study the Earth's climate variability on seasonal to decadal time scales and to  
33 assess future scenarios from changes in anthropogenic forcing when coupled with the ice,  
34 atmosphere, and land components of the climate system, and to generate short-term ocean forecasts  
35 or long-term reanalysis when integrated in a data-assimilation framework. These applications offer  
36 valuable insights on various aspects of the ocean circulation and its role in the Earth's climate.

37 Due to finite computational resources and discretized equations of motion, not all processes  
38 can be accurately represented in OGCMs and some of them need to be parameterized. Thus, the  
39 OGCM's horizontal and vertical grid spacing is and will remain the fundamental parameters for  
40 any configuration. For example, the horizontal grid spacing determines to what extent an ocean  
41 model can resolve mesoscale eddies, which represents close to 80% of the ocean kinetic energy  
42 (Richardson, 1983; Klein et al., 2019). At  $1^\circ$  (coarse resolution), mesoscale eddies are not  
43 permitted and need to be parameterized. At  $1/10^\circ$  (eddy resolution), there is a reasonable  
44 representation of the mid-latitude western boundary currents and associated mesoscale eddies (e.g.,  
45 Paiva et al., 1999; Smith et al., 2000; Hallberg, 2013) and their impacts on large-scale circulation  
46 in global/basin scale simulations is now well-recognized (e.g., Chassignet et al., 2020; Hirschi et  
47 al., 2020; Roberts et al., 2020). When the horizontal grid spacing approaches 1 km (sub-mesoscale  
48 enabling resolution), ocean models not only resolve mesoscale eddies, but also start to resolve

49 some sub-mesoscale features at mid- and low-latitudes. The impact of resolving sub-mesoscale  
50 variability on large-scale ocean circulation has been highlighted by Hurlburt and Hogan, (2000),  
51 Lévy et al. (2010), Chassignet and Xu (2017), and Chassignet et al. (2023).

52 In contrast to the rich literature quantifying the impact of the horizontal resolution on ocean  
53 circulation, few studies have discussed the impact of vertical resolution. The early studies (Adamec,  
54 1988; Weaver and Sarachik, 1990; Barnier et al., 1991) were performed with either a quasi-  
55 geostrophic model or OGCMs with relatively low vertical resolution. The importance of vertical  
56 resolution was revisited recently by Stewart et al. (2017) who state that the purpose of the vertical  
57 grid in a hydrostatic OGCM is to resolve the vertical structure of the horizontal flows (rather than  
58 to resolve vertical motions), and that vertical grids should be constructed to represent baroclinic  
59 modal structures to complement and not undermine the theoretical capabilities of a given  
60 horizontal grid. Stewart et al. (2017) suggest that for  $z$ -coordinate global ocean models, at least 50  
61 well-positioned vertical levels are required to resolve the first baroclinic mode, with an additional  
62 25 levels per subsequent mode. They showed that, when vertical resolution is increased from 50  
63 to 75 levels, a  $1/10^\circ$  global ocean simulation gains some dynamical enhancements, including  
64 substantial increases in the sea surface height (SSH) variance and eddy kinetic energy (EKE) as  
65 well as in the magnitude of the overturning streamfunction associated with the Antarctic Bottom  
66 Water (AABW).

67 It is, however, important to point out that the increases in SSH variance/EKE and overturning  
68 strength in Stewart et al. (2017) when using 75 levels are most noticeable in the southern high  
69 latitudes (see their Figures 9 and 10) where the  $1/10^\circ$  horizontal resolution only partially resolves  
70 the first baroclinic mode (Hallberg, 2013) and does not resolve the second baroclinic mode.  
71 Furthermore, a recent study by Ajayi et al. (2020, 2021) show that having “only 32 isopycnal layers

72 was not detrimental to the representation of the dynamics in the ocean interior” when comparing  
73 two sub-mesoscale enabled North Atlantic simulations with drastically different vertical  
74 resolutions: one  $1/60^\circ$ , 300-level NEMO (a  $z$ -level model) and the other  $1/50^\circ$ , 32-layer HYCOM  
75 (a hybrid coordinate ocean model with isopycnic coordinates in the stratified interior). A  
76 comparison of the vorticity spectral coherence as a function of depth showed that the two  
77 simulations are essentially identical in terms of the depth penetration of energetic eddy structures.  
78 Besides resolving baroclinic modes, the vertical resolution in OGCMs serves another fundamental  
79 purpose, i.e. an accurate representation of water masses and associated water mass transformation.  
80 The question then arises as to whether the dynamical enhancements of Stewart et al. (2017) are  
81 indeed truly due to a better representation of the second baroclinic mode with the additional 25  
82 levels or to the addition of levels that better discretize the high latitude water masses and allow for  
83 more accurate dense water formation (i.e., the AABW in Stewart et al. (2017)).

84 In this paper, we document and quantify the impact of the vertical resolution on the ocean  
85 circulation and water mass representation when using both  $z$ -levels and constant density layers  
86 (i.e., isopycnals) as the vertical coordinate. The main difference between  $z$ -level and layer  
87 (isopycnal) models is the ability of the latter to differentiate and keep track of distinct water masses,  
88 with the caveat that potential density surfaces are not exactly neutral, especially in high latitudes  
89 (see Stanley, 2019 for discussion on neutral surface). First, in section 2, we argue that vertical  
90 resolution is unlikely to undermine the capability of a given horizontal grid in representing the  
91 vertical modes. Both the 50 well-positioned  $z$  levels as in Stewart et al. (2017) and the standard  
92 32-layer HYCOM configuration are adequate choices to represent the zero-crossing of first five  
93 baroclinic modes in mid-latitudes as well their vertical structure. Subsequently, in section 3, we  
94 investigate the impact of the vertical resolution choices on water mass representation and the

95 circulation in a series of 1/12° North and Equatorial Atlantic configurations using isopycnic  
 96 coordinates. Specifically, we find that the 24-, 32-, 64-, and 96-layer configuration all exhibit  
 97 similar large-scale North Atlantic surface circulation and Atlantic meridional overturning  
 98 circulation, whereas the 16-layer simulation is unable to accurately represent dense overflow  
 99 waters. These findings are summarized, and their implications are discussed in section 4.

## 100 2. Vertical Mode Representation in $z$ -level and Isopycnic Coordinates

### 101 2.1. Horizontal Resolution and the Baroclinic Rossby Radii of Deformation

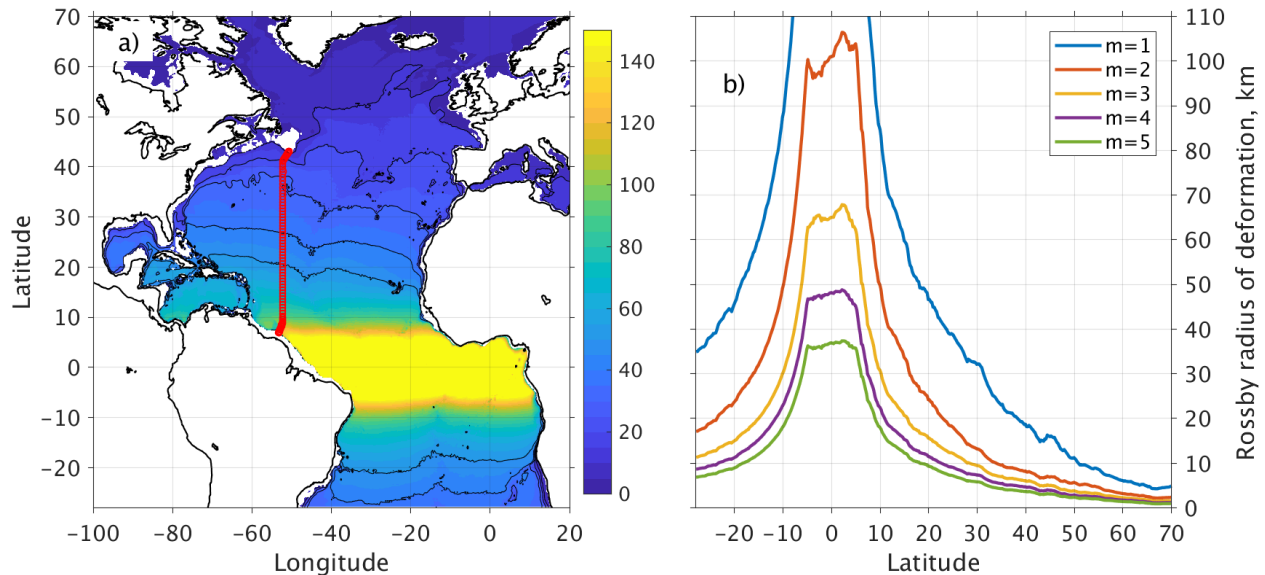
102 Before discussing how a specific baroclinic mode is resolved by the vertical grid, it is useful  
 103 to first review the minimum horizontal grid spacing that is needed to resolve the corresponding  
 104 baroclinic Rossby radius of deformation (Rossby radius hereafter) and associated physical  
 105 processes in an OGCM. Figure 1 displays the spatial distribution of the first baroclinic Rossby  
 106 radius in the North and Equatorial Atlantic Ocean computed from the annual mean density profiles  
 107 of an ocean climatology (Chelton et al., 1998), and the zonally averaged Rossby radii for the first  
 108 five baroclinic modes as a function of latitude. The Rossby radius and the vertical structure of the  
 109 baroclinic modes are obtained by solving a Sturm-Liouville eigenvalue problem (e.g., Chelton et  
 110 al., 1998; Hallberg, 2013; Stewart et al., 2017) with the Rossby radius,  $\lambda_m$ , for mode- $m$  defined as

$$111 \quad \lambda_m = \sqrt{\frac{c_m^2}{(f^2 + 2\beta c_m)}} \quad (1)$$

112 and the corresponding baroclinic wave phase speed,  $c_m$ , defined as

$$113 \quad c_m \approx \frac{1}{m\pi} \int_{-H}^0 N(z) dz. \quad (2)$$

114  $f$  and  $\beta$  are the Coriolis parameter and its meridional derivative, respectively, and  $N(z)$  is the  
 115 Brunt-Väisälä frequency.



116  
 117 **Figure 1.** a) First baroclinic Rossby radius of deformation (in km) in the North and Equatorial  
 118 Atlantic Ocean as computed from the density profiles of the ocean climatology-Generalized  
 119 Digital Environment Model (GDEM, Carnes 2009). The black contours in the North Atlantic from  
 120 south to north are 50, 40, 30, 20, and 10 km, respectively. The red circles indicate location of the  
 121 WOCE line A20 along which high-resolution hydrographic surveys are conducted. b) Zonally  
 122 averaged Rossby radii for the first five baroclinic modes.

123 The first Rossby radius is in the order of 20-40 km at mid-latitude but decreases to less than  
 124 10 km in the subpolar North Atlantic because of an increasing Coriolis parameter and decreasing  
 125 stratification. If we assume that a minimum of two grid points is needed within the Rossby radius  
 126 to resolve the first baroclinic mode, i.e., Hallberg (2013), thus, an eddying resolution of  $1/12^\circ$  ( $\sim 6$   
 127 km) does resolve the first baroclinic mode at mid-latitudes, but barely in the weakly stratified high  
 128 latitude ocean. However, if we adopt Soufflet et al. (2016)'s concept of an effective resolution,  
 129 which depends on the OGCM's inherent numerical dissipation and is on the order of  $6\Delta x$ , then  
 130  $1/12^\circ$  ( $\sim 6$  km) barely resolves the first baroclinic mode at mid-latitudes. Considering that  $1/50^\circ$   
 131 ( $\sim 1.5$  km) represents the finest horizontal resolution currently used in OGCMs (Uchida et al., 2022)  
 132 and that the Rossby radius for the  $m^{\text{th}}$  baroclinic mode is approximately the first baroclinic Rossby  
 133 radius divided by  $m$ , current sub-mesoscale enabled OGCMs are only able to resolve up to the fifth  
 134 baroclinic Rossby radius at mid-latitudes if one adopts Hallberg (2013)'s  $2\Delta x$  criterion and even

135 less with Soufflet et al. (2016)'s  $6\Delta x$  criterion. Subsequently, in the remainder of this paper, we  
136 focus only the representation of the first five baroclinic modes.

## 137 **2.2. Vertical Resolution and the Baroclinic Rossby Radii of Deformation**

138 In theory, the first baroclinic mode for a given density profile can be represented as a two-layer  
139 system with one zero-crossing interface. Thus, over a given domain, it is reasonable to expect that  
140 only a few z-levels or density layers should be able to provide a reasonable representation of the  
141 first Rossby radius, provided that the spatial variation of the density and corresponding interface  
142 depth are small. We test this hypothesis over the North and Equatorial Atlantic by computing the  
143 first Rossby radius using a) 78-level GDEM climatology (Figure 1a) as the reference, b) 2, 3, and  
144 4 fixed z-levels (derived from the spatially averaged zero-crossing depths of the 1<sup>st</sup>, 2<sup>nd</sup>, and 3<sup>rd</sup>  
145 baroclinic mode, respectively), and c) 2, 3, and 4 isopycnic layers (derived from the spatially  
146 averaged densities above and below the zero-crossing depths of the 1<sup>st</sup>, 2<sup>nd</sup>, and 3<sup>rd</sup> baroclinic mode,  
147 respectively). Figure 2 shows the error in the first Rossby radius,  $E(R_m)$ , calculated using 2 to 4  
148 levels or layers when compared to that of calculated from the 78-level climatology (Figure 1a).

$$149 \quad E(R_m) = \frac{R_m^{low} - R_m^{clim}}{R_m^{clim}}, \quad (3)$$

150 in which  $R_m^{clim}$  is the Rossby radius for mode  $m$  calculated from 78-level GDEM climatology  
151 (Figure 1a), and  $R_m^{low}$  from the lower vertical resolution configurations. A minimum of 2 levels or  
152 layers is required to compute the first baroclinic Rossby radius. When two levels are defined using  
153 the spatially averaged zero-crossing depth of the first mode (1170 m, see Table A1 in the  
154 Appendix), the error in the first Rossby radii is on the order of 10% to 20% over most of the  
155 domain and is higher in the tropics (Figure 2a). It is significantly less when using 2 isopycnic

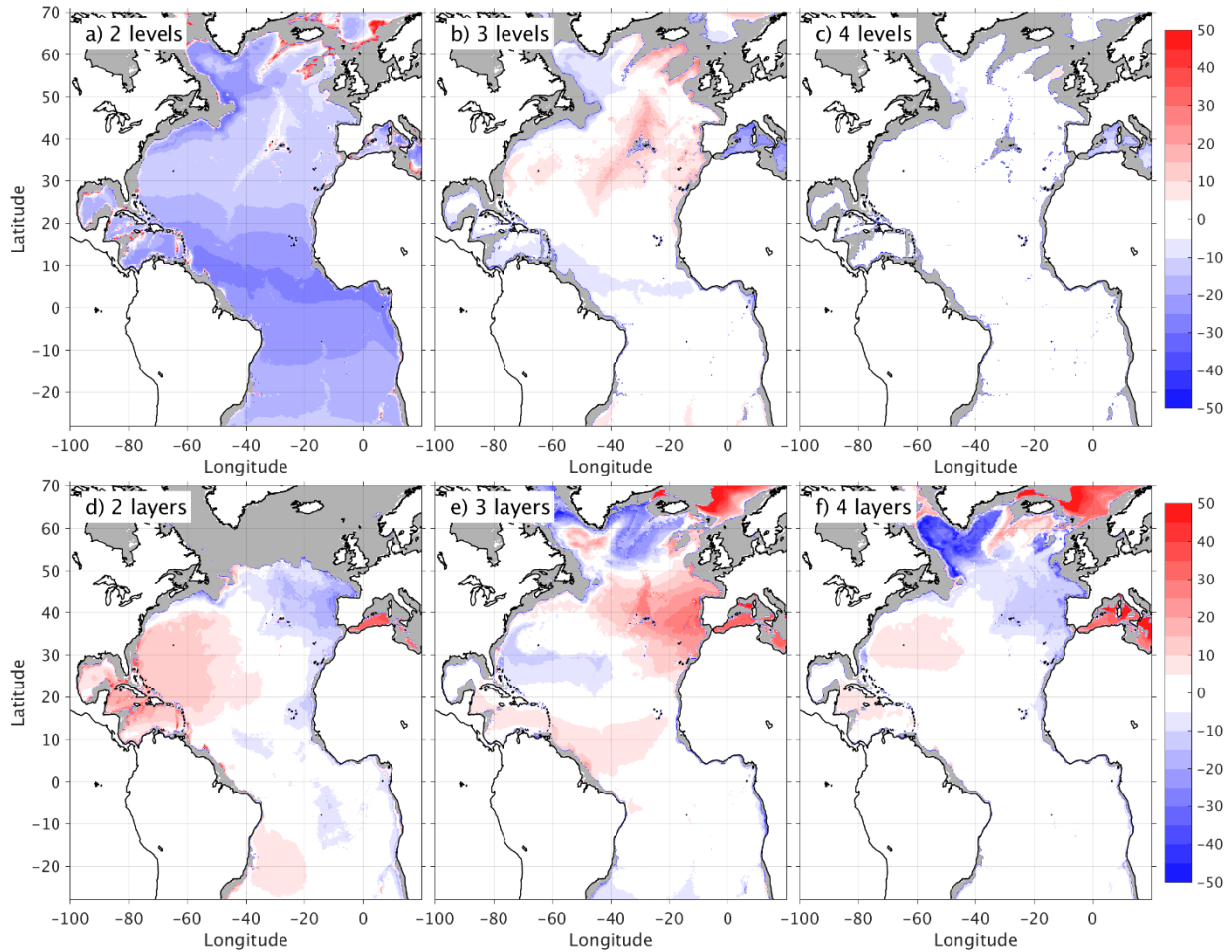


156 layers ( $\sigma_2$  densities of 35.80 and 36.96 kg/m<sup>3</sup>, see table A2 in the Appendix) (Figure 2d), especially  
157 in the tropics. The main reason is that for most of the Equatorial/mid-latitude region, a 2-layer  
158 configuration defined by the permanent pycnocline is a good approximation of the density profile.  
159 It does not perform as well at higher latitudes in unstratified regions. As one increases the number  
160 of levels or layers, the error in the Rossby radius drops quickly and, in the Equatorial/mid-latitude  
161 region, it is very small (less than 5%) with 4 levels or 4 layers.

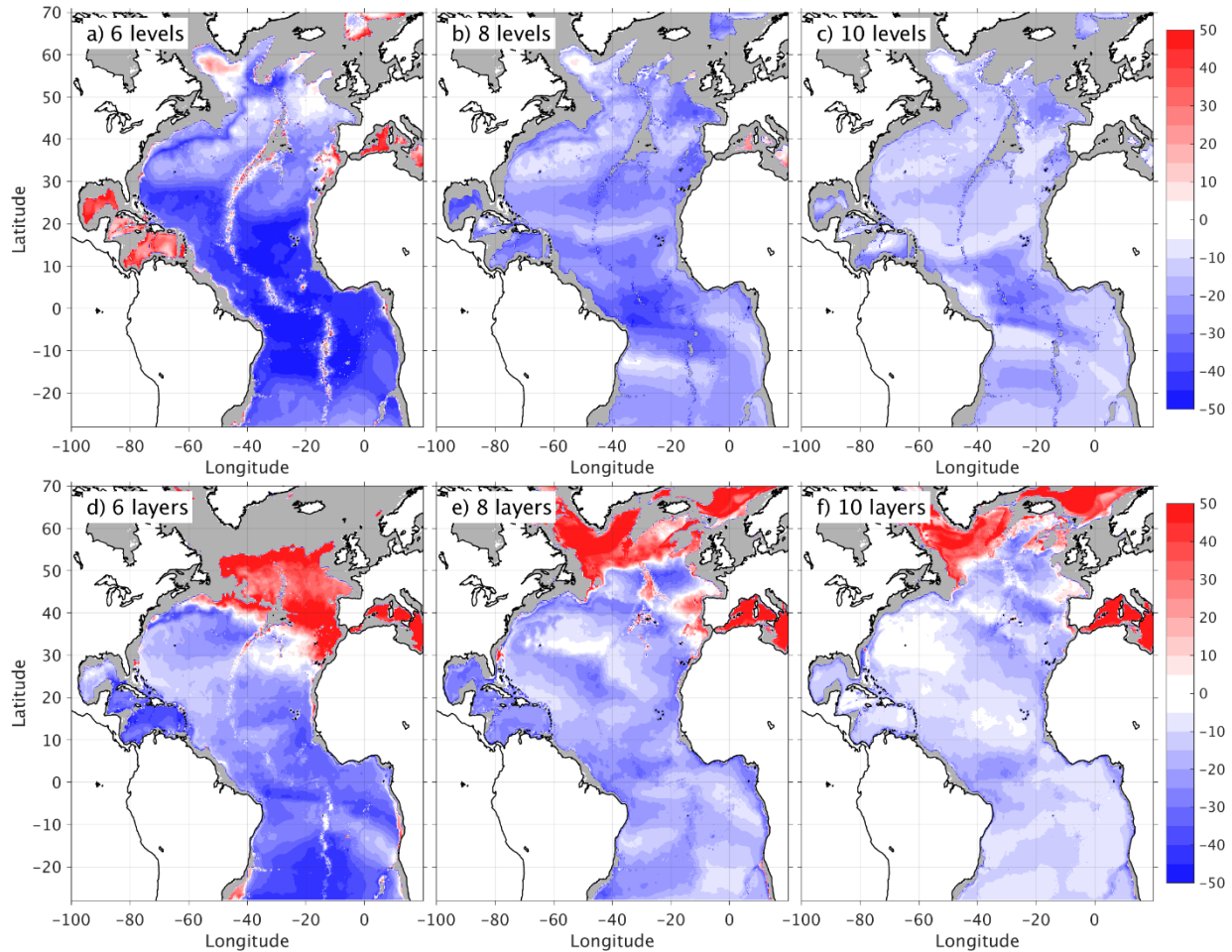
162 One can repeat this exercise for higher modes. Figure 3 displays the error in the fifth Rossby  
163 radii calculated for 6, 8, and 10 levels and 6, 8, and 10 layers, respectively (the z-levels and  
164 isopycnic layer densities are listed in the Appendix in Tables A1 and A2), when compared to the  
165 Rossby radii calculated from the GDEM climatology. A minimum of 6 levels/layers is required to  
166 compute the fifth Rossby radius and the percentage error is higher (on the order of 50% for the z-  
167 levels, less for the layer configuration) than for the first Rossby radius defined by 2 levels/layers  
168 (Figure 2). As for the first Rossby radius (Figure 2), the error also decreases as the vertical  
169 resolution increases, but at a slower pace. With 10 levels/layers, the error is in the order of 15-20%.

170 Overall, the results shown in Figures 2 and 3 confirm the premise that one does not require that  
171 many levels or layers to represent the first five Rossby radius over most of the deep ocean. This,  
172 however, does not mean that such a low-resolution vertical grid can be applied to a basin scale or  
173 global model. For example, one cannot define two levels in regions when the depth is less than the  
174 spatially averaged zero-crossing depth (or when density at bottom is lower than the spatially  
175 averaged density). These areas are shown in gray in Figures 2 and 3. In addition, surface water is  
176 denser in high latitude than in the tropical region, thus some isopycnals (defined by spatially  
177 averaged density) outcrops to the surface in the subpolar region and the effective number of

178 isopycnic layers is reduced (e.g., the unstratified regions in the subpolar North Atlantic). In the  
 179 overflows, both coordinate systems fail to represent mode 1 processes.



180  
 181 **Figure 2.** Error (in %) in the first Rossby radius of deformation calculated from 2, 3, and 4 levels  
 182 (a-c) and 2, 3, 4 isopycnic layers (d-f) when compared to the Rossby radius of deformation  
 183 calculated from GDEM4 climatology. Blue/red color indicates where the low vertical resolution  
 184 configuration under-/overestimates the first Rossby radius. Gray areas indicate regions where the  
 185 Rossby radius cannot be computed (depth too shallow or non-existing density). Levels and layer  
 186 densities are provided in Tables A1 and A2 of the Appendix,



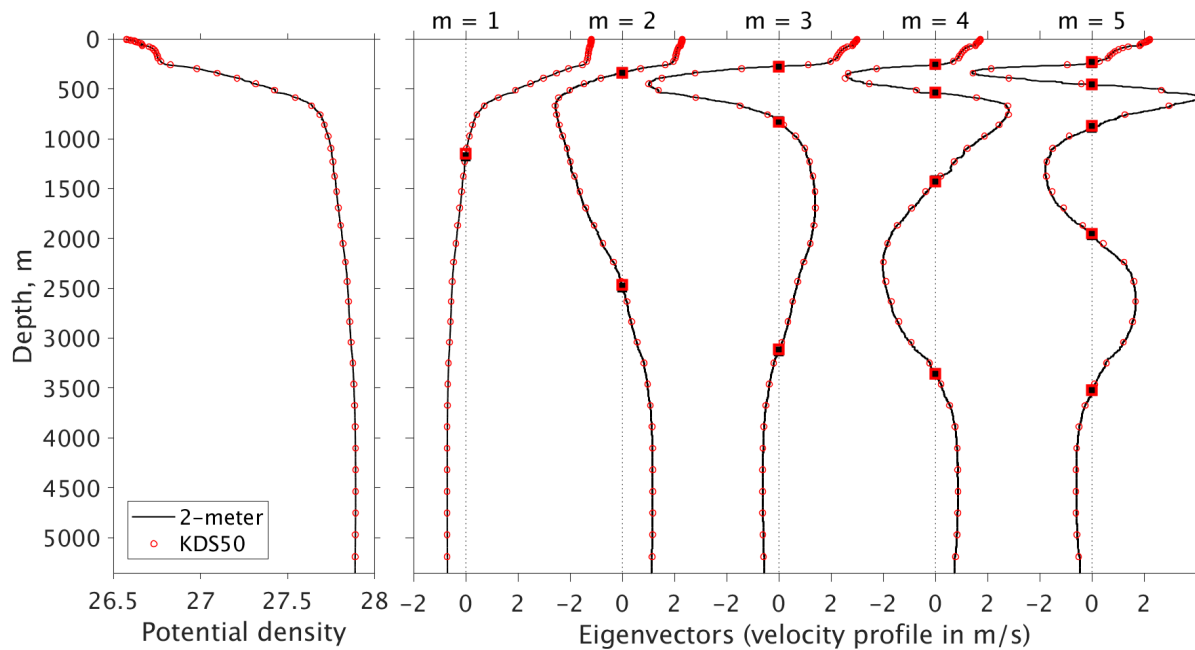
187

188 **Figure 3.** Difference (in %) between the fifth Rossby radius of deformation calculated from  
 189 GDEM, from 6, 8, and 10 levels (a-c), and 6, 8, and 10 isopycnic layers (d-f). Blue/red color  
 190 indicates where the low vertical resolution configuration under-/over-estimates the fifth Rossby  
 191 radius of deformation. Gray areas indicate regions where the Rossby radius cannot be computed  
 192 (depth too shallow or non-existing density). Levels and layer densities are provided in Tables A1  
 193 and A2 of the Appendix,

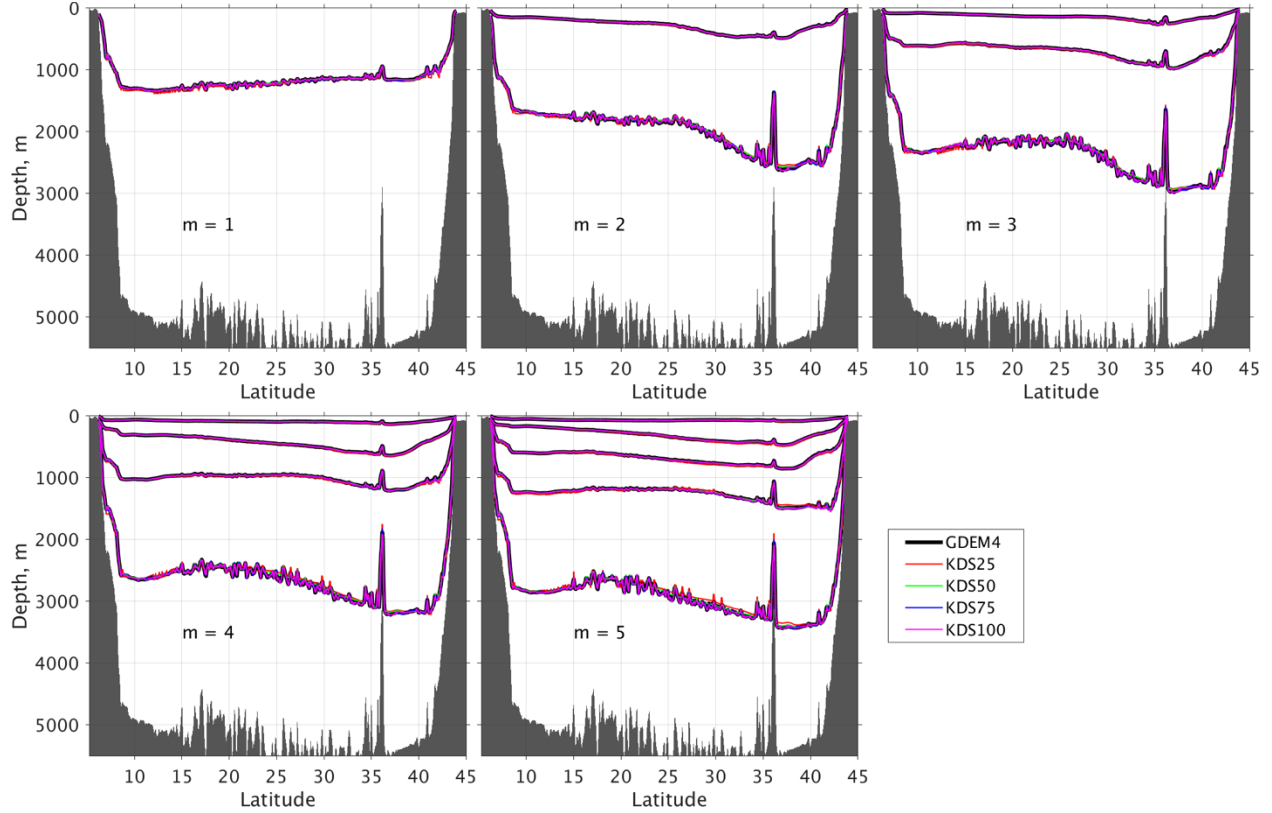
### 194 2.3. Baroclinic Mode Representation in OGCMs

195 A proper representation of the baroclinic Rossby radii is a measure of how well the model can  
 196 represent the phase speed of the first baroclinic mode or the total stratification of the water column  
 197 using the WKB approximation (Chelton et al., 1998; Stewart et al., 2017). In addition to ensuring  
 198 that the vertical grid provides the right Rossby radii (focus of the previous section), one could also  
 199 argue that the vertical structure of the baroclinic modes themselves needs to be resolved (Stewart

200 et al., 2017). In this section, we evaluate the ability of vertical grids commonly used in OGCMs  
 201 to do so. The left panel of Figure 4 shows a single density profile near 40°N from the World Ocean  
 202 Circulation Experiment (WOCE) line A20 where the black line is the original 2-m resolution CTD  
 203 data and the red circles represent the profile using the KDS50 grid of Stewart et al. (2017) (varying  
 204 grid spacing from 2.7 m near the surface to 219 m near the bottom). The right panel shows the  
 205 corresponding vertical profile of the first five baroclinic modes calculated from the 2-m resolution  
 206 and the KDS50 grid, respectively. There is no loss of information when using the KDS50 grid for  
 207 all five modes, with nearly identical velocity profile and zero-crossing depth (Figure 4). Similar  
 208 result can be found for other stations along the section.



209  
 210 **Figure 4.** (Left panel) potential density profile of potential density at a station near 40°N along the  
 211 WOCE line A20 (red circles in Figure 1), black line is of 2-m resolution and red-circle is in KDS50  
 212 grid in Stewart et al. (2017), with 53 levels from 2.7 m near surface to 219 m at a maximum depth  
 213 of 5363 m. (Right panel) the corresponding velocity profile of the first five baroclinic modes based  
 214 on 2-m resolution (black line) and KDS50 grid (red circles), with zero-crossing depth marked by  
 215 squares for the 2-m resolution (black) and the KDS50 grid (red).



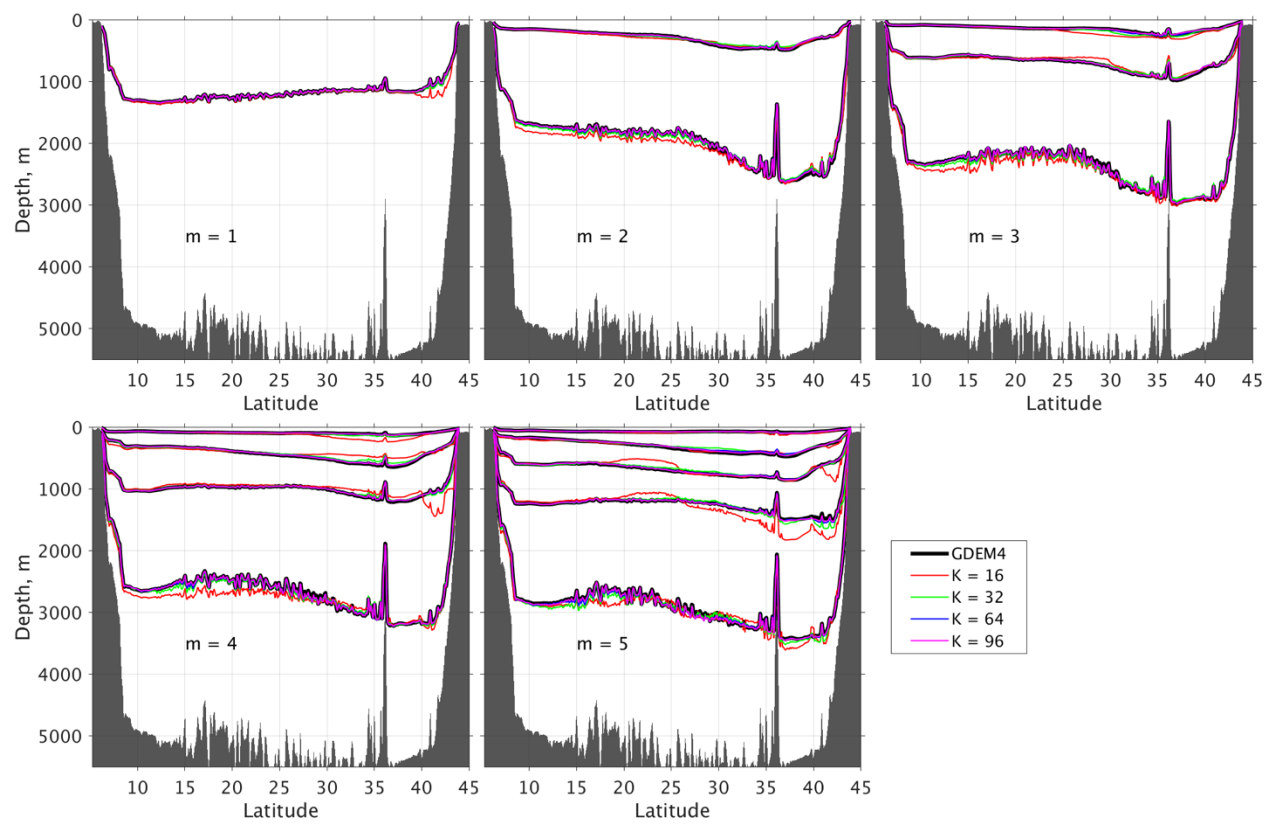
216  
 217 **Figure 5.** Zero-crossing depth of the first five baroclinic modes along 52°W based on the ocean  
 218 climatology GDEM (black lines) and four z-levels configurations with KDS25 (red), KDS50  
 219 (green), KDS75 (blue), and KDS100 (magenta).

220 To assess how well the vertical mode structure is represented in an OGCM grid, Figure 5  
 221 displays the distribution of zero-crossing of the first five modes computed from the GDEM  
 222 climatology and four z-levels configurations, KDS50, KDS75, and KDS100 in Stewart et al.  
 223 (2017), and KDS25 that is defined as half of the resolution KDS50 (by merging every two levels  
 224 into one). The results show that all four OGCM grid represent the zero-crossing well. One way of  
 225 quantifying the differences is to calculate a normalized error,  $\overline{E(h_{m,k})}$ , as in Stewart et al. (2017)  
 226 in zero-crossing depths between the climatology and the OGCMs' vertical grids.

227

$$\overline{E(h_{m,k})} = \frac{|h_{m,k}^{clim} - h_{m,k}^{OGCM}|}{h_{m,k}^{clim}}, \quad (4)$$

228 in which  $h_{m,k}^{clim}$  and  $h_{m,k}^{OGCM}$  are the depth of the  $k^{th}$  zero-crossing for the  $m^{th}$  mode as represented  
 229 in climatology and in OGCM resolution, respectively. The averaged error for the full section is  
 230 less than 10% for KDS25, and 2% for the other three grids. The small error is not too surprising  
 231 as a hindsight, because the GDEM climatology itself is 78-level, thus the error in the KDS75 and  
 232 KDS100 is essentially rounding error introduced by re-gridding and interpolating.



233 **Figure 6.** Zero-crossing depth of the first five baroclinic modes along 52°W based on the ocean  
 234 climatology GDEM (black lines) and four isopycnic configurations with 16 (red), 32 (green), 64  
 235 (blue), and 96 (magenta) layers.

237 The next step is to assess how well the vertical mode structure is represented in OGCMs with  
 238 isopycnic coordinates. Figure 6 displays the zero-crossing depths of the first five baroclinic modes  
 239 along A20 line near 52°W represented in four configurations with 16, 32, 64, and 96 layers used  
 240 in the North and Equatorial Atlantic HYCOM configuration. The standard 32-layer configuration  
 241 has been used extensively by Xu et al. (2010, 2012, 2014, 2022), Chassignet and Xu (2017, 2021),

242 and Chassignet et al. (2023). The selection of isopycnic layers was adapted from a previous global  
 243 simulation and was modified to represent the key water masses in the Atlantic Ocean, especially  
 244 the deep dense water masses (see Xu et al., 2012). The 16, 64, and 96 layers were constructed by  
 245 either collapsing layers or splitting the layers in two or three from the original 32-layer  
 246 configuration. The 16-layer configuration represents the first and second modes reasonably well,  
 247 but not the higher modes (Figure 6) in part because of its shallower first interface depth (Eq. 4),  
 248 whereas the 32, 64, and 96-layer configurations represent the zero-crossing depths of all five  
 249 modes to a good approximation. The normalized errors along the A20 section for all 15 zero-  
 250 crossing depths of the first five modes are less than 10% for the 32-layer configuration and less  
 251 than 5% for the 64 and 96-layer configurations (Table 1).

252 **Table 1.** The average error (in %) of the zero-crossing depth along A20. The error is defined as  
 253 the normalized difference between the zero-crossing depth as calculated from the GDEM4  
 254 resolution and from OGCMs grids: four z-level configurations (KDS25, KDS50, KDS75, and  
 255 KDS100) and four layer configurations with 16, 32, 64, and 96 layers.

	m=1	m=2	m=3	m=4	m=5
KDS25	2.1	2.9; 1.7	4.1; 2.0; 1.6	5.7; 2.2; 1.7; 1.7	7.4; 4.0; 2.3; 1.7; 1.8
KDS50	0.8	0.8; 1.1	1.1; 0.7; 1.1	1.5; 0.8; 0.6; 1.0	1.5; 0.8; 0.7; 0.6; 0.8
KDS75	0.7	0.7; 0.7	1.1; 0.7; 0.7	1.2; 0.7; 0.6; 0.6	1.0; 0.8; 0.7; 0.6; 0.5
KDS100	0.5	0.6; 0.6	0.8; 0.6; 0.5	0.9; 0.7; 0.4; 0.4	0.7; 0.9; 0.6; 0.6; 0.4
K=16	3.2	8.8; 4.8	22.6; 5.8; 3.5	31.6; 11.9; 7.3; 4.4	18.3; 8.1; 8.2; 9.7; 3.5
K=32	0.6	5.1; 1.9	8.1; 2.0; 1.5	7.3; 4.4; 1.4; 1.4	5.2; 5.5; 3.0; 2.6; 1.8
K=64	0.2	2.2; 0.6	2.5; 0.8; 0.5	3.1; 1.8; 0.5; 0.5	4.5; 4.0; 1.2; 0.8; 0.7
K=96	0.3	1.5; 0.4	2.0; 0.8; 0.4	3.1; 1.4; 0.4; 0.3	4.3; 2.7; 0.8; 0.7; 0.5

256

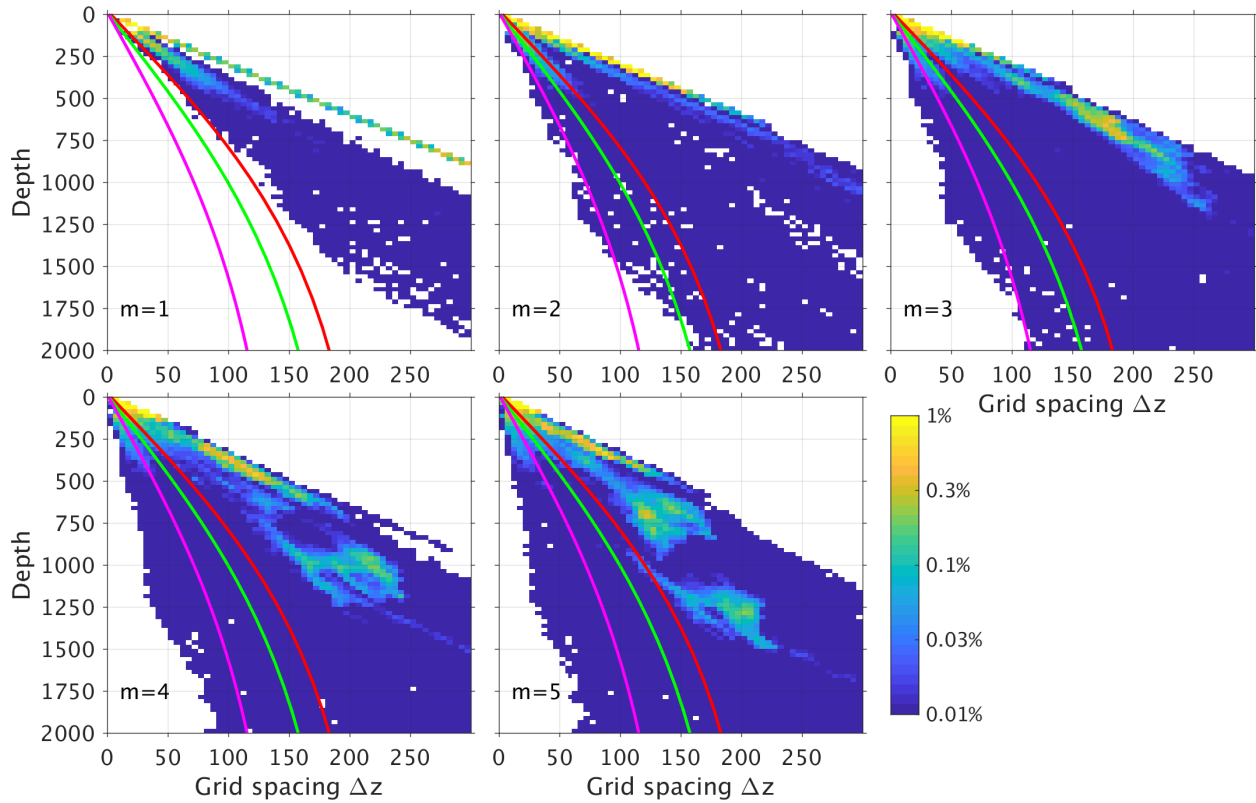
## 257 **2.4. Vertical Grid Spacing Requirements in z-levels versus Isopycnic Layers**

258        Stewart et al. (2017) evaluates the ability of a vertical grid to represent the vertical modes by  
259 comparing the distribution of the model vertical grid spacing against the  $\Delta z$  requirement to resolve  
260 a specific mode. The latter is defined as 1/3 of the distance between zero-crossing depths in order  
261 to have a minimum of 3 grid points (see their Figure 6). Figure 7 reproduces Figure 6 of Stewart  
262 et al. (2017), but for the first 5 modes and for the GDEM climatology in the North and Equatorial  
263 Atlantic. As in Stewart et al. (2017), we find that, for the first mode, all vertical grid spacing  
264 profiles (KDS50, KDS75, and KDS100) lie to the left of the data points, therefore meeting the  
265 resolution requirements (Stewart et al., 2017). For the second mode, only the 100-level vertical  
266 grid profile lies to the left. For the third, fourth, and fifth modes, there are some data lies to the left  
267 of the profile, but they only represent a small fraction of the total. We can repeat the same exercise,  
268 but this time in density space (Figure 8). The 16-layer configuration meets most of the first and  
269 second modes requirements, but there are quite some data points lying to the left of the profile for  
270 the higher modes. The second mode is well represented with 32 and higher number of layers, but  
271 one would need 64 or 96 layers to fully satisfy the requirements of the third and higher modes.

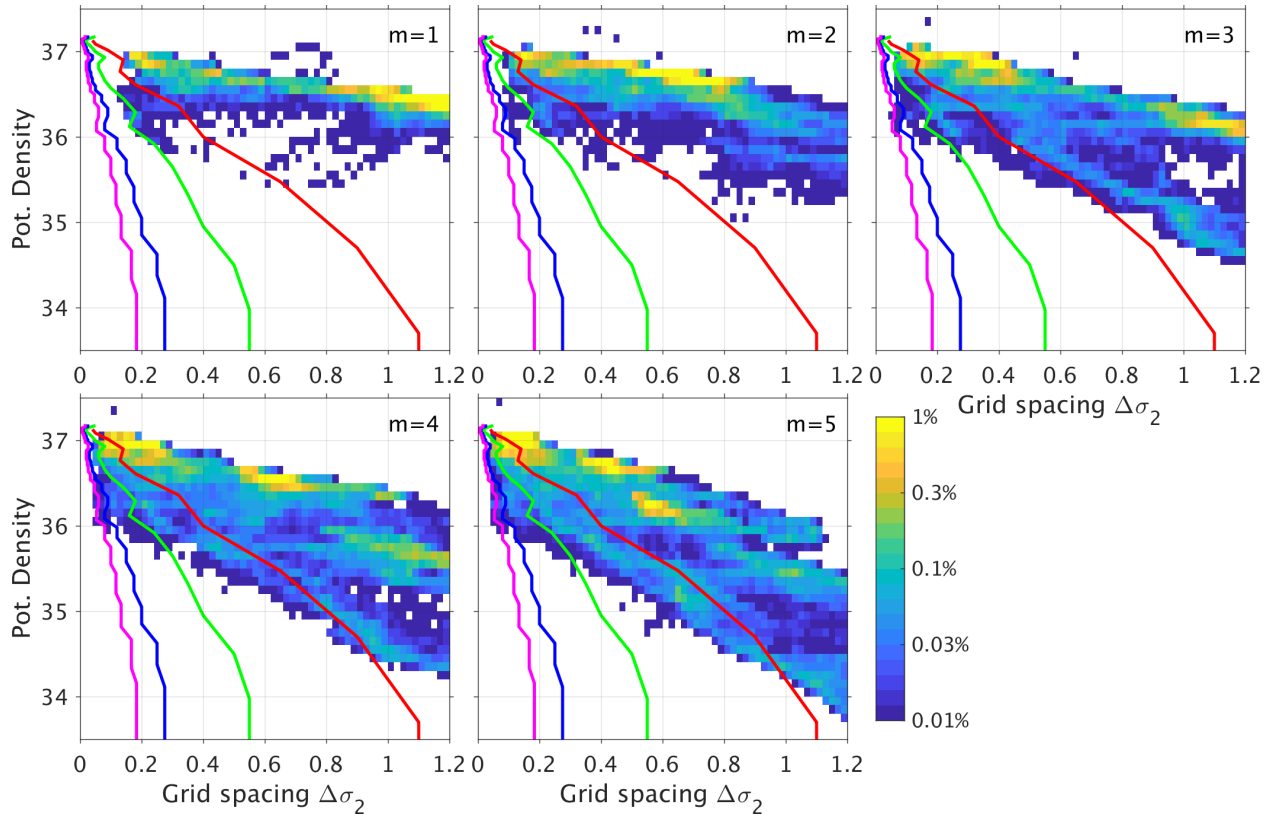
272        In summary, we argue that the vertical resolution used in current OGCMs (50-75 levels or 30-  
273 40 layers) adequately represents the first two modes (zero-crossing depths and vertical grid  
274 requirement), but that there is definitely an advantage in using density layers instead of levels in  
275 representing higher modes. A 100-level configuration cannot satisfy Stewart et al. (2017)'s grid  
276 requirement for the first five modes while a 96-layer configuration does. This is primarily because  
277 a minimum of three levels is required in z-coordinate model to represent a single water mass versus  
278 only one constant density layer in isopycnic coordinate models, thus giving a factor of three



279 advantage to the latter. Isopycnic coordinate models are also not constrained by the vertical grid  
 280 when representing the bottom bathymetry.



281  
 282 **Figure 7:** Probability distribution (color shading) of the grid spacing  $\Delta z$  needed to resolve the first  
 283 five baroclinic modes in the Atlantic Ocean as a function of depth compared to the vertical grid  
 284 defined for KDS50 (red), KDS75 (green), and KDS100 (magenta) as defined in Stewart et al.  
 285 (2017). To fully resolve the baroclinic mode, there should be no  $\Delta z$  distribution to the left of the  
 286 colored lines.



287  
 288 **Figure 8.** Probability distribution (color shading) of the density spacing (in  $\sigma_2$ ) needed to resolve  
 289 the first five baroclinic modes in the Atlantic Ocean as a function of potential density, compared  
 290 to the vertical density grid defined for 16 (red line), 32 (green line), 64 (blue line), and 96 (magenta  
 291 line) layers. To fully resolve the baroclinic mode, there should be no density spacing distribution  
 292 to the left of the colored lines.

### 293 3. Impact of Vertical Resolution on Water Mass Representation in the North Atlantic.

294 Being able to represent vertical modes accurately in a OGCM is only one aspect of choosing a  
 295 vertical grid. The other constraint is being able to model the different water masses present  
 296 throughout the ocean as well as the associated water mass transformations. While this was not the  
 297 main purpose of the Stewart et al. (2017) study as it focused on modes, they did however include  
 298 some water mass considerations when constructing their vertical grid (i.e., the minimum and  
 299 maximum thickness near the surface and bottom). In this section, we not only investigate the  
 300 impact of the vertical resolution on the ocean circulation from a baroclinic modal decomposition  
 301 point of view, but also from a water mass representation perspective. This is achieved by

302 performing a series of North and Equatorial Atlantic numerical simulations (28°S to 80°N) with  
303 varying vertical and horizontal grid spacing. The main reason for focusing on the North Atlantic  
304 is that the domain size is much more affordable computationally than the global domain, therefore  
305 allowing for the exploration vertical grid sensitivity over a wide range (from 16 to 96 layers).  
306 Furthermore, the North Atlantic is one of the most observed ocean basins (e.g., Frajka-Williams  
307 et al., 2019; Lozier et al., 2019), an important consideration when evaluating the realism of the  
308 model solutions. All simulations are performed with the Hybrid Coordinate Ocean Model  
309 (HYCOM; Bleck, 2002; Chassignet et al., 2003), in which the vertical coordinate is isopycnic in  
310 the stratified open ocean and makes a dynamically smooth and time-dependent transition to terrain  
311 following in shallow coastal regions and to fixed pressure levels in the surface mixed layer and/or  
312 unstratified seas. In doing so, the model combines the advantages of the different coordinate types  
313 in simulating coastal and open ocean circulation features simultaneously (Chassignet et al., 2006).  
314 The North and Equatorial Atlantic configuration is well documented; see Chassignet and Xu (2017)  
315 and the references therein. Details of the model configurations are provided in the Appendix.

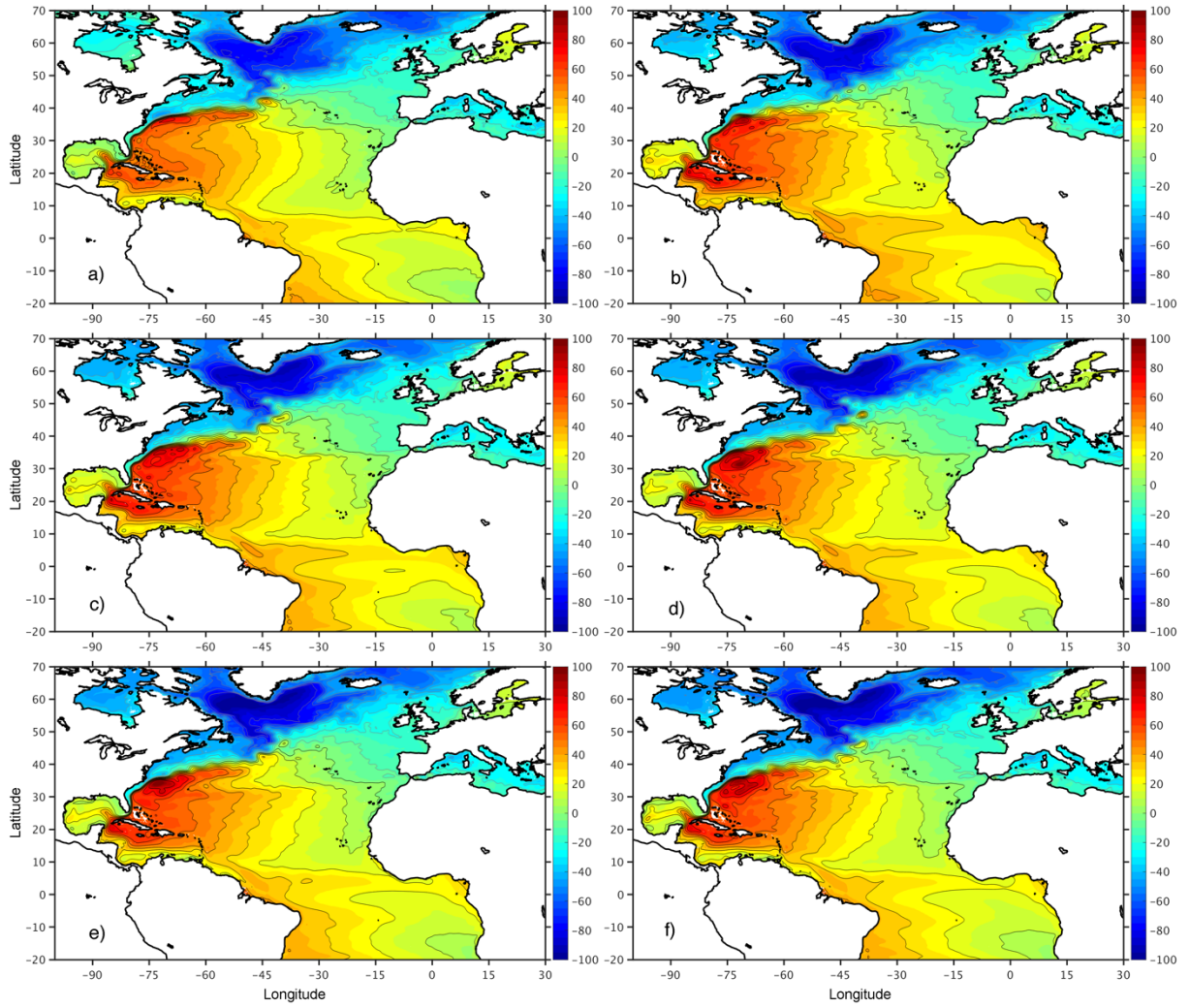
### 316 **3.1 Time Mean and Variability of the Surface Circulation.**

317 The time mean sea surface height (SSH) and its variability are displayed in Figures 9 and 10,  
318 respectively. Figure 9a is the latest CNES-CLS18 mean dynamic topography (MDT, Mulet et al.,  
319 2021), which is calculated from a combination of altimeter and space gravity data and  
320 oceanographic in-situ measurements (i.e., drifting buoy velocities, hydrographic profiles). The  
321 subtropical and subpolar gyres (represented by the sub-basin scale positive and negative anomalies,  
322 respectively), the western boundary current of the Florida Current, the Gulf Stream, and the North  
323 Atlantic Current (represented by the contracted MDT contours), as well as the Azores current near  
324 35°N extended from 45°W to the Strait of Gibraltar can all be easily identified. The modeled

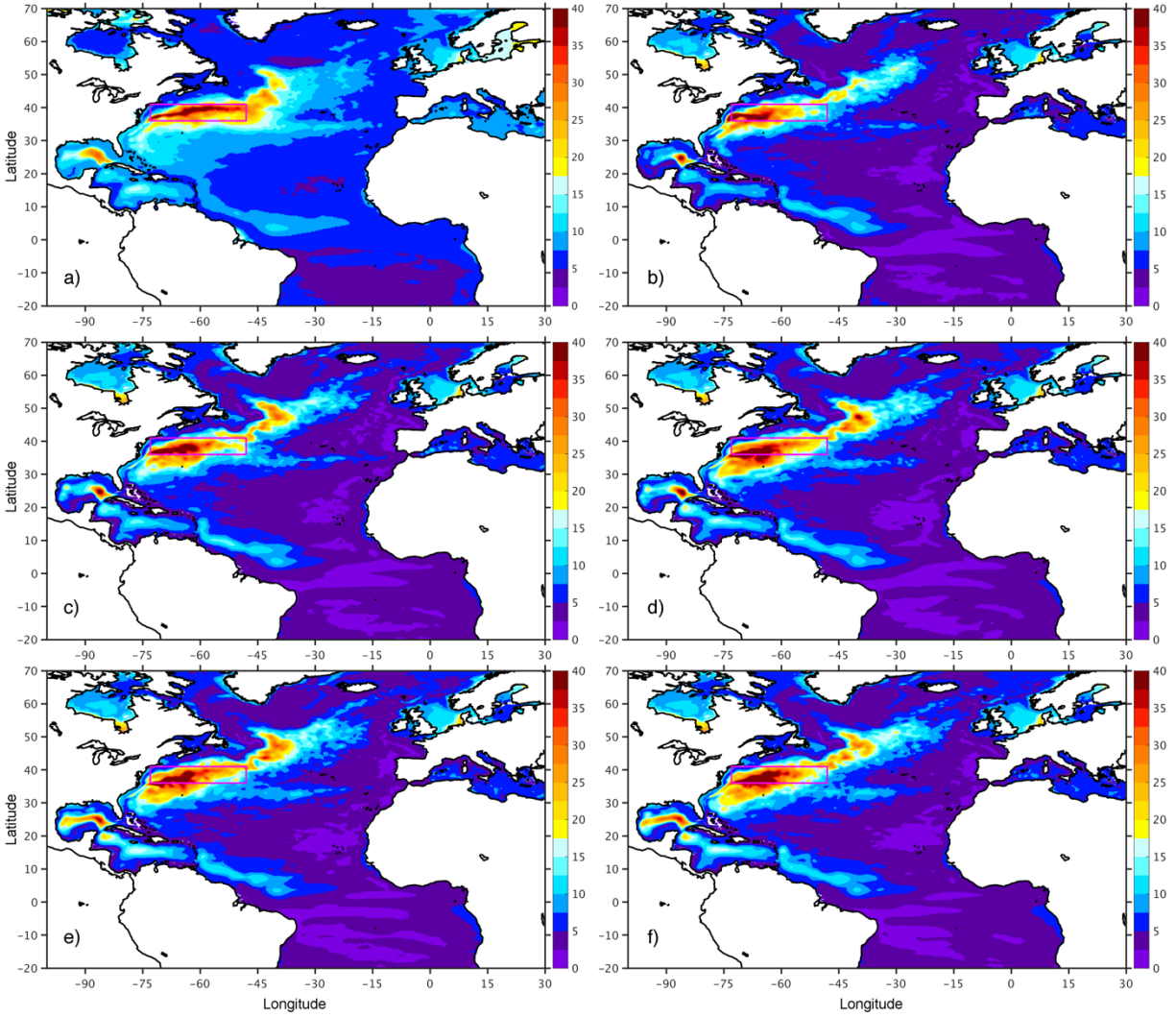
325 circulation is similar to the observations from a large-scale perspective but differs in its details.  
326 The most noticeable difference between the observations and the model results is probably in the  
327 representation of the Gulf Stream and North Atlantic Current. At  $1/12^\circ$ , the modeled Gulf Stream  
328 does not extend far enough to the east and its southern recirculation is confined to the west of about  
329  $65^\circ\text{W}$  (Chassignet and Xu, 2017). Among the five simulations, the 16-layer simulation (Figure 9b)  
330 has the worst representation of the North Atlantic circulation with a northward Gulf Stream  
331 separation and a poor representation of the North Atlantic Current northwest corner near  $52^\circ\text{N}$ .  
332 The 16-layer simulation also has a weaker and shallower AMOC recirculation cell (discussed in  
333 the following section). Overall, the surface circulation in the other four simulations is similar to  
334 each other and an increase to 96 layers does not lead to a significantly change in surface circulation.

335 The kinetic energy of the ocean circulation is dominated by mesoscale eddies that are most  
336 active in the western boundary current system: the North Brazil Current, the Loop current, the  
337 Florida Current, the Gulf Stream, and the North Atlantic Current (Figure 10a). While all five  
338 simulations represent this observed broad pattern well, there are some clear differences. Overall,  
339 the variability in the interior is lower in the models than in the observations. This is a common  
340 feature of models, even with finer horizontal resolution, which is attributed to the coarse resolution  
341 (space and time) atmospheric forcing (Chassignet and Xu, 2017; Chassignet et al., 2020). For the  
342 energetic western boundary current associated with the Gulf Stream, the modeled SSH variability  
343 has a wider area of high variability meridionally to the west of about  $65^\circ\text{W}$  and is weaker to the  
344 east of this longitude. As shown in Chassignet and Xu (2017), this is associated with the Gulf  
345 Stream not penetrating enough to the east at this resolution ( $1/12^\circ$ ) and the results are drastically  
346 improved when the horizontal resolution is increased to  $1/50^\circ$ . To provide a simple quantitative  
347 measure of the Gulf Stream SSH variability, we calculated the SSH standard deviation in a  $25 \times 5^\circ$

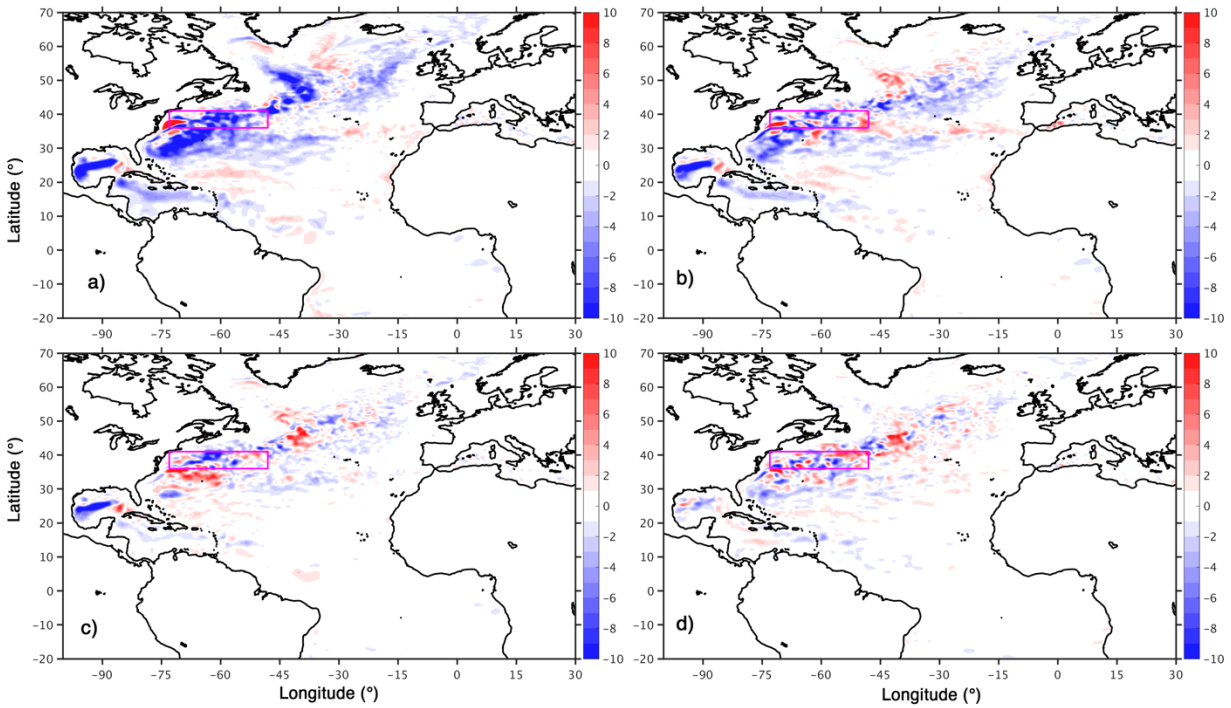
348 box of 73-48°W, 36-41°N (magenta rectangle in Figure 10). The area-averaged standard deviation  
349 value is 25.6 cm in observation (Figure 10a), compared to 21.4, 23.7, 24.0, 24.9, and 25.2 cm for  
350 the five experiments of 16, 24, 32, 64, and 96-layer, respectively (Figures 10b-f). The 10% increase  
351 from the 16- to the 24-layer simulation, although smaller than that in Stewart et al. (2017), may be  
352 representative of a better representation of the baroclinic mode as discussed in section 2. The  
353 increase takes place in mid-latitude where the first Rossby radius is fully resolved by the 1/12°  
354 horizontal resolution. From 24 to 96-layer, the SSH variability continues to increase, but at a  
355 smaller pace, with a 6% increase in SSH variability for a 4-fold increase in the number of layers.  
356 The similarity or difference in modeled SSH variability is shown in Figure 11, which displays the  
357 difference in SSH variability from the 16- to 64-layer configurations when compared to the 96-  
358 layer configuration. The 16-, 24- and, to a lesser degree, the 32-layer configurations clearly show  
359 a lower variability in the Gulf Stream and in the Gulf of Mexico, whereas the 64-layer  
360 configuration has a similar variability, when compared to the 96-layer reference. This is in general  
361 consistent with the point made in section that the baroclinic modes that are allowed by the  
362 horizontal resolution are better represented in the 64- and 96-layer simulations.



363  
 364 **Figure 9.** A comparison of observed and modeled time mean surface circulation: a) the  
 365 CNES\_CLS18 mean dynamic topography MDT (in cm, from Mulet et al., 2021), b-f) the 5-year  
 366 mean modeled sea surface height (SSH, in cm) from five  $1/12^\circ$  Atlantic HYCOM simulations with  
 367 16, 24, 32, 64, and 96 layers, respectively.



368  
 369 **Figure 10.** A comparison of observed and modeled surface circulation variability: the standard  
 370 deviation value of the sea surface height (SSH, in cm) from a) satellite altimetry data (1993-2018)  
 371 distributed by Copernicus Marine Environment Monitoring Services (CMEMS) and b-f) five  $1/12^\circ$   
 372 Atlantic HYCOM simulations with 16, 24, 32, 64, and 96 layers, respectively.



373  
 374 **Figure 11.** Difference in the standard deviation of the sea surface height (SSH, in cm) in a) 16-  
 375 layer, b) 24-layer, c) 32-layer, and d) 64-layer  $1/12^\circ$  Atlantic HYCOM simulations compared to  
 376 the 96-layer HYCOM simulation. Blue color indicates lower SSH variability compared to 96-layer  
 377 simulation.

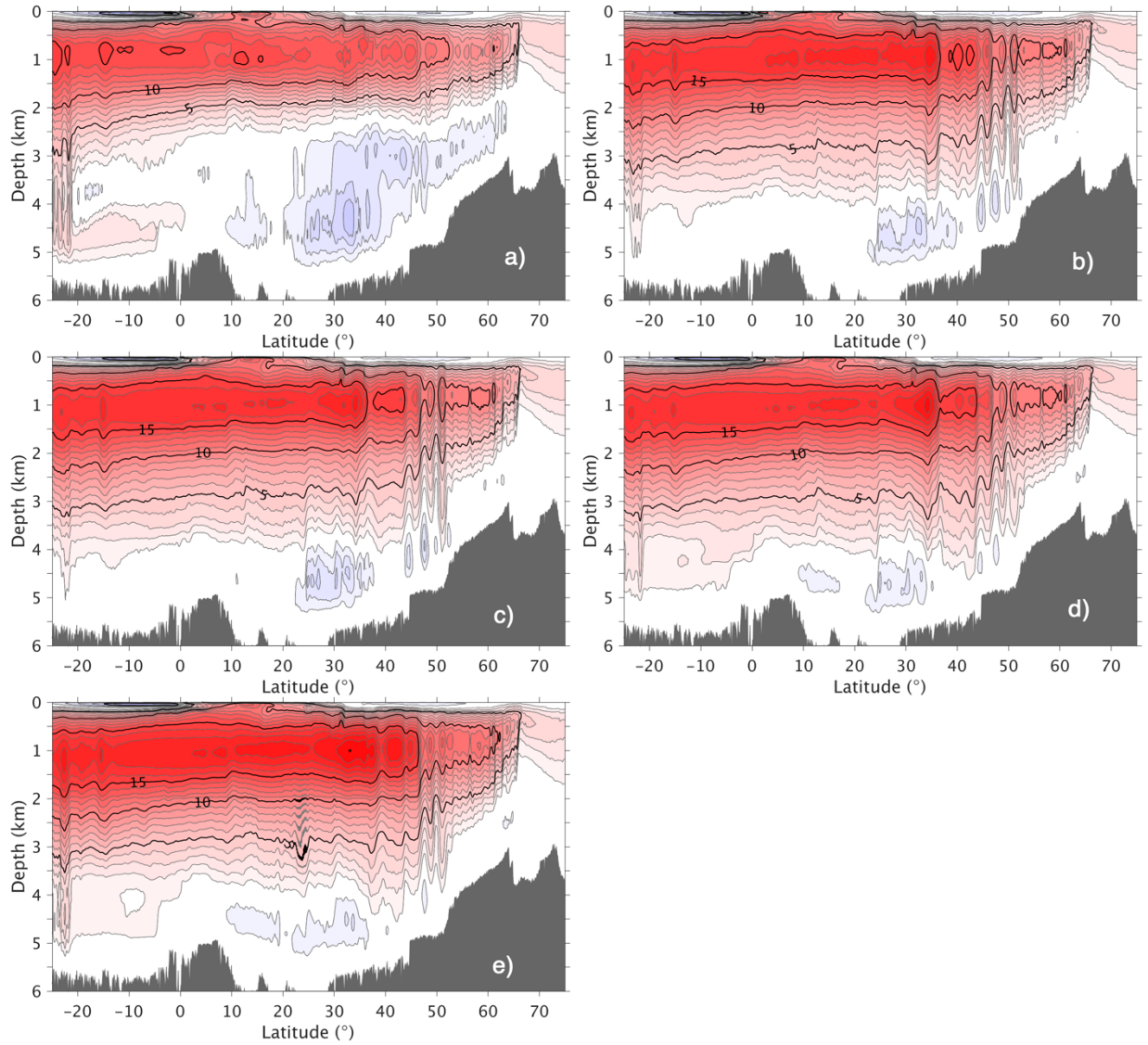
### 378 3.2. AMOC in the Subtropical and Subpolar North Atlantic

379 The AMOC consists of a northward flow of warm, saline water in approximately the upper 1  
 380 km and a southward flow of colder, fresher North Atlantic Deep Water below this depth (which is  
 381 also roughly the depth of permanent pycnocline and hence the zero-crossing for the first baroclinic  
 382 mode in the mid-latitude). Thus, it might be reasonable to expect some connections between the  
 383 representation of the AMOC, the mode, and the vertical resolution. The large-scale AMOC is often  
 384 defined by an overturning streamfunction  $\psi_z$ , which is calculated at a given latitude as the  
 385 integrated meridional transport (Sv) across the basin from surface to a given depth  $z$ . The modeled  
 386 streamfunction  $\psi_z$  as a function of latitude is shown in Figure 12 for the five simulations: it shows  
 387 a northward flow in the upper 1 km or so throughout the entire domain from the South Atlantic to

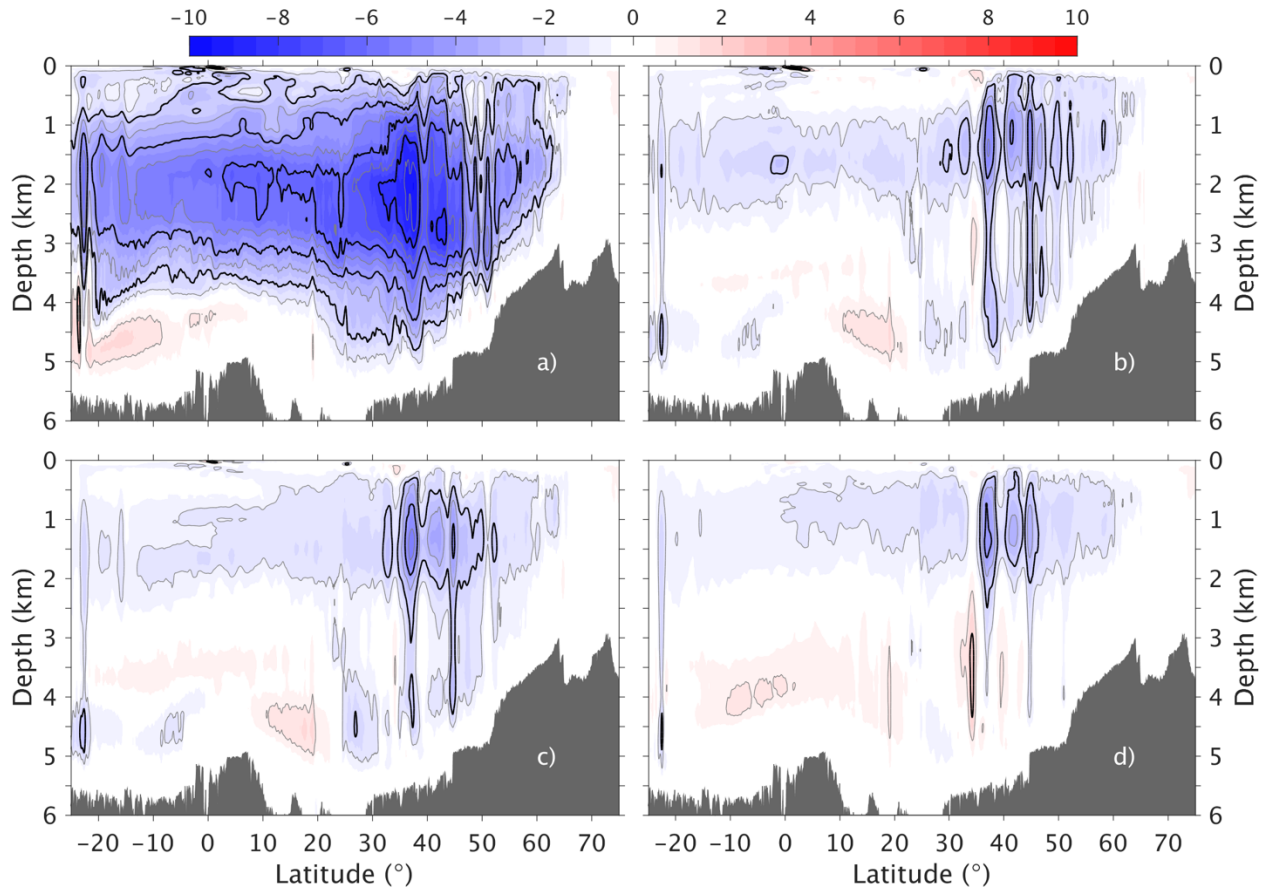


388 about 60°N in the North Atlantic, and southward flow of North Atlantic Deep Water (NADW)  
389 below this depth. The most important result from Figure 12 is that the AMOC structure is  
390 qualitatively similar in the four simulations with 24, 32, 64, and 96 layers, but that the 16-layer  
391 simulation exhibits a weaker AMOC with no southward flow below 2500 m, an indication of  
392 lacking dense overflow water contribution (which will be seen clearer in the streamfunction  
393 defined in density coordinate discussed later). The 24-layer simulation (Figure 12b), which has the  
394 same upper layer distribution as in the 16-layer and a lower layer distribution as in the 32-layer,  
395 shows similar results to the 32-layer simulation (Figure 12c). The difference in the modeled  
396 AMOC streamfunctions  $\psi_z$  is displayed in Figure 13, with the 96-layer simulation used as a  
397 reference. The overturning strength increases with finer vertical resolution, with a maximum  
398 difference at mid-latitudes. The largest difference in streamfunction is more than 8 Sv for the 16-  
399 layer simulation when compared to the 96-layer, but this is reduced to 2-4 Sv in the other three  
400 simulations (24, 32, and 64 layers).

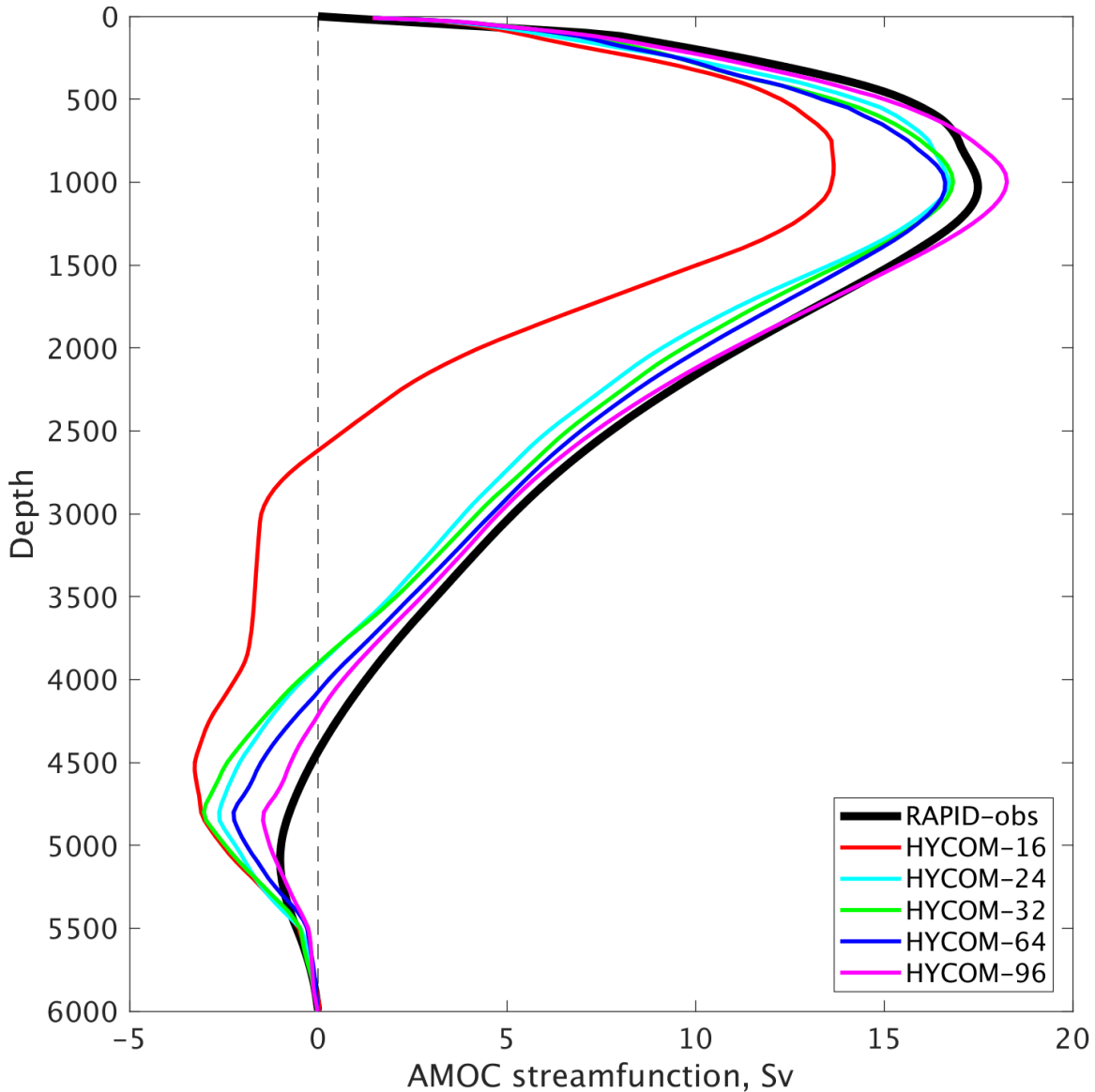
401 To compare the modeled AMOC structure and observations quantitatively, Figure 14 displays  
402 the streamfunction  $\psi_z$  at 26.5°N. The black line from the updated RAPID line observations (e.g.,  
403 Smead et al., 2018), and the colored lines represent the modeled streamfunction for the five  
404 simulations. The results highlight that, at this latitude, the 16-layer simulation has a weaker time-  
405 mean AMOC (14 versus 17 Sv) and that the southward component of NADW is too shallow (2600  
406 versus 4500 m). The other four simulations have a time mean AMOC magnitude close to the  
407 observations (difference of about 1 Sv). As the vertical resolution increases, the modeled  
408 southward NADW component becomes deeper and much closer to the observations. This  
409 highlights that increased vertical resolution leads to a better representation of the water masses  
410 comprising the AMOC (e.g., NADW).



411  
 412 **Figure 12.** Modeled time mean meridional overturning streamfunction (in Sv) as a function of  
 413 depth ( $z$ ) and latitude in five  $1/12^\circ$  Atlantic HYCOM simulations with different vertical resolutions:  
 414 a) 16, b) 24, c) 32, d) 64, and e) 96 layers, respectively. The results show that expect the 16-layer  
 415 simulation, the other four simulations have an overall similar overturning streamfunction structure.



416  
 417 **Figure 13.** Difference in modeled time-mean meridional overturning streamfunction (in Sv) as a  
 418 function of depth and latitude in four  $1/12^\circ$  Atlantic HYCOM simulations with a) 16, b) 24, c) 32,  
 419 and d) 64 layers, respectively, compared to the 96-layer simulation as a reference. Blue color  
 420 indicates streamfunction value is lower in the low-resolution simulation and vice versa. The gray  
 421 and black contours are with 1 and 2 Sv interval, respectively.



422

423 **Figure 14.** Time mean meridional overturning streamfunction (in Sv) across the RAPID array near  
 424 26°N from observations and five 1/12° Atlantic HYCOM simulations with different vertical  
 425 resolutions from 16 to 96 layers. The results show that expect the 16-layer simulation, the other  
 426 four simulation show a similar overturning streamfunction as the observations.

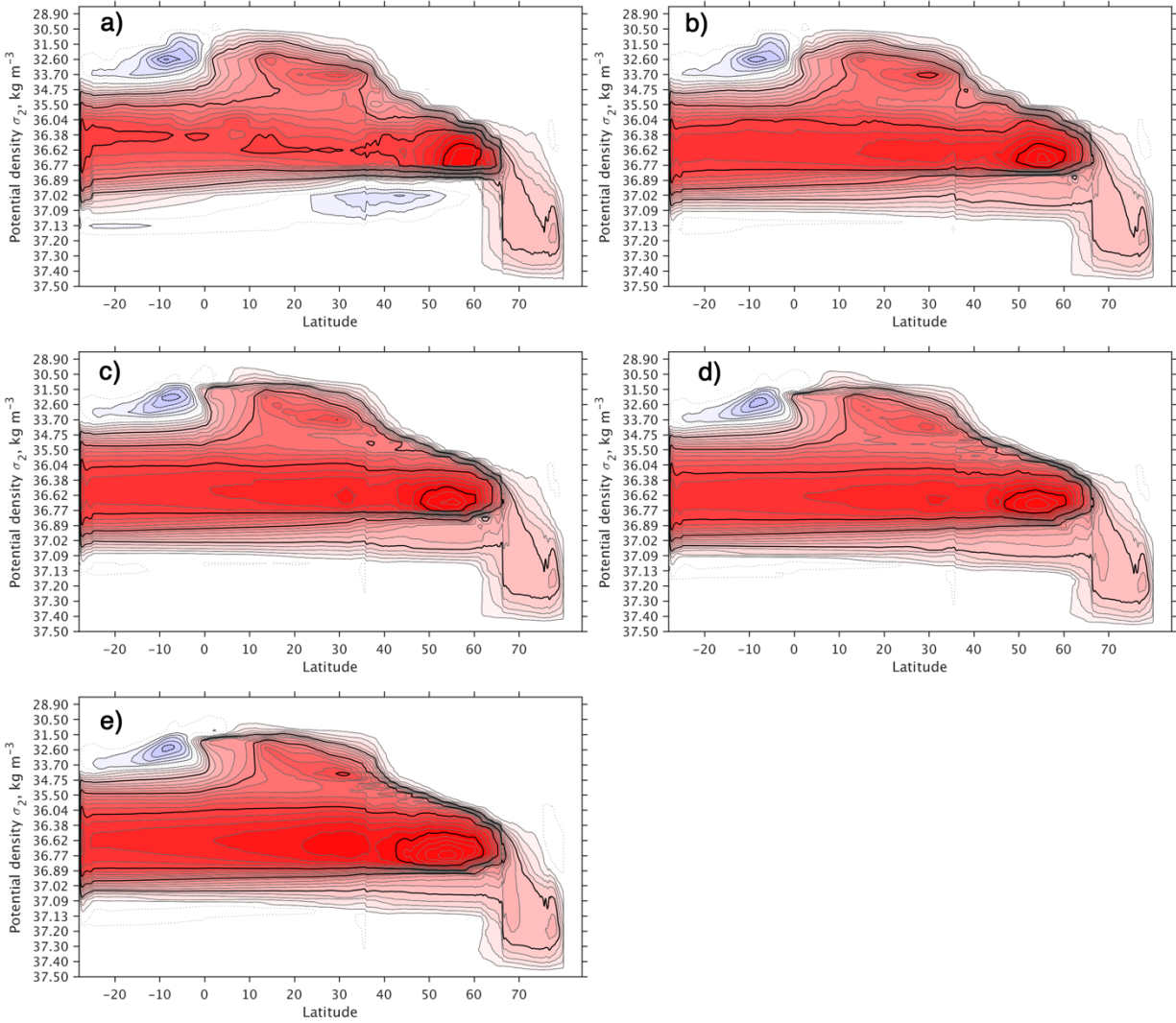
427 The AMOC is also evaluated in streamfunction with respect to density  $\psi_\sigma$ , which is defined as  
 428 the integrated meridional transport (Sv) across the basin above a constant density surface. The  $\psi_\sigma$   
 429 connects directly to water mass transformation (Xu et al., 2018) and is more useful in describing  
 430 the AMOC in the high latitude where the northward and southward components, along the eastern  
 431 and western side of the basin, respectively, takes place at a similar depth, but on different density

432 surface (due to the sloping isopycnic surface across the basin in the northern latitudes). Figure 15  
433 shows the streamfunction  $\psi_\sigma$  from these simulations. The picture is similar to that in Figure 12, in  
434 that the four higher resolution simulations show a qualitatively consistent structure of overturning  
435 streamfunction, including both the basin-scale AMOC, and smaller sub-basin scale overturning in  
436 the subtropical (centered near  $30^\circ\text{N}$  and  $34 \text{ kg/m}^3$ ) and subpolar (centered near  $55^\circ\text{N}$  and  $36.77$   
437  $\text{kg/m}^3$ ). The latter represents the diapycnal transformation associated with the subtropical/subpolar  
438 gyres; see Xu et al. (2016; 2018) for more discussions. As for  $\psi_z$  streamfunctions, the 16-layer  
439 simulation exhibits a somewhat similar structure to the higher vertical resolution simulations in  
440 the northward-flowing part of the streamfunction, but the overturning strength is much weaker and  
441 the southward component does not have any overflow water contribution south of the  $65^\circ\text{N}$ . This  
442 indicates that, due to lack of vertical resolution, the modeled overflow water is not well represented  
443 with thick shallow layers and becomes part of LSW after spilling over the sill. The overflow water  
444 masses underwent a significant density change from its source to final product water downstream  
445 (e.g., Legg et al. 2009), and the vertical resolution in the 16-layer configuration is too coarse for  
446 that transformation. A similar deficiency can be found in a regional modeling of the Mediterranean  
447 outflow when vertical resolution is too coarse (Xu et al., 2007).

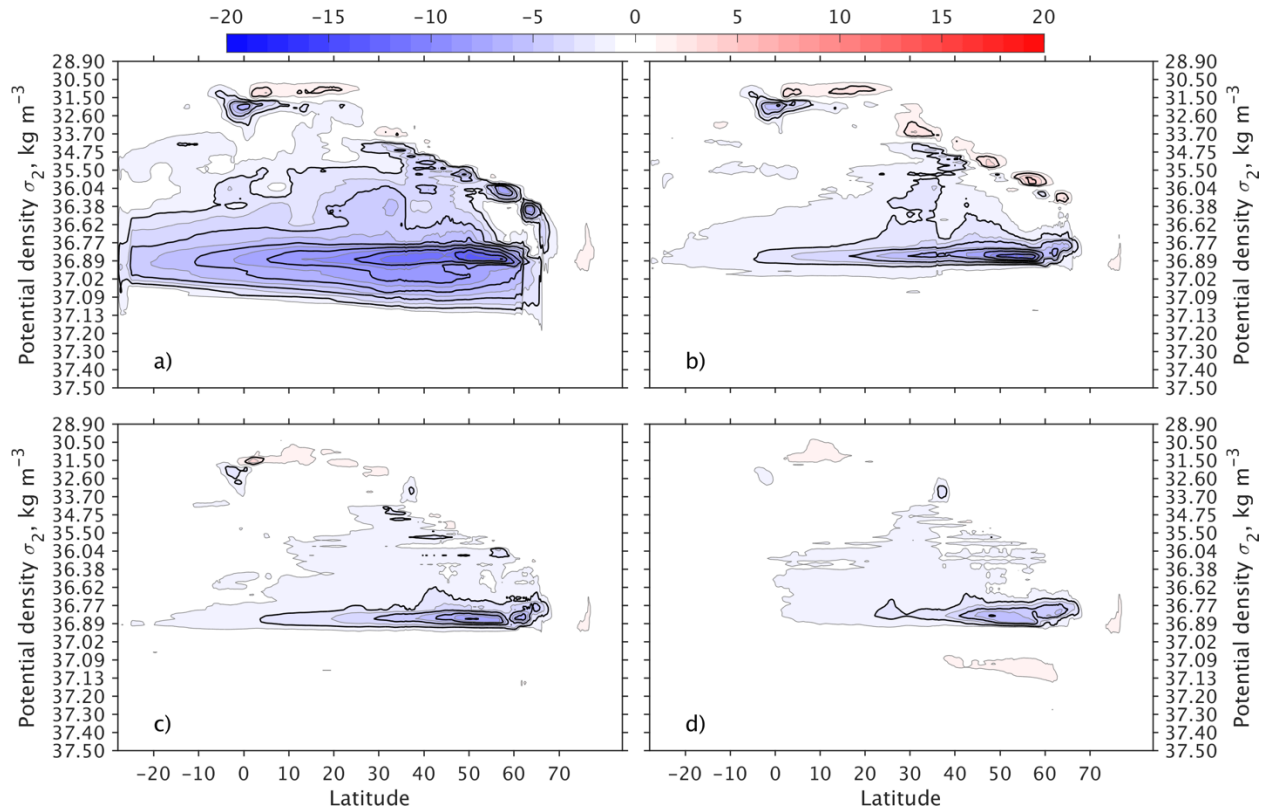
448 As in Figure 14, Figure 16 displays the difference in overturning streamfunction, but in density  
449 coordinate. Here the results also show a lower streamfunction value in the coarser vertical  
450 resolution (16- to 64-layer) simulations and the difference is mostly centered near the LSW density  
451 range (i.e., the blue patch centered in near  $36.77\text{-}36.89 \text{ kg/m}^3$ ). The magnitude of difference as  
452 defined in density coordinate, from more than 12 Sv in 16-layer to 6 Sv in 64-layer, is about 2  
453 times of that in  $z$ -coordinate. It should be emphasized that the differences in Figure 16 in

454 streamfunctions is not so much about a stronger or weaker overturning, but more about the  
455 overturning streamfunctions on a slightly lighter/denser density.

456 Like the RAPID observations in the subtropical region, the OSNAP observations (Lozier et al.,  
457 2019) provided a benchmark to quantitatively evaluate the modeled AMOC structure in the  
458 subpolar North Atlantic, where the NADW is formed. Figure 17 compares the density structure of  
459 the AMOC for both the western section from Labrador to Greenland, eastern section from  
460 Greenland to Scotland, and combined full sections (see Figure A1 in the appendix for locations).  
461 When the OSNAP section is considered as a whole, all model simulations produce stronger  
462 overturning than observed, with more LSW and similar transport of overflow water (Figure 17a).  
463 The stronger overturning is attributed mostly to a stronger overturning across the western section  
464 as the overturning across the eastern section is comparable between model and observations  
465 (Figures 17b-c). When the model sensitivity is considered, the four simulations (24- to 96-layer)  
466 show a similar transformation structure, whereas the 16-layer simulation lacks a contribution from  
467 the dense overflow water (Figure 17b).



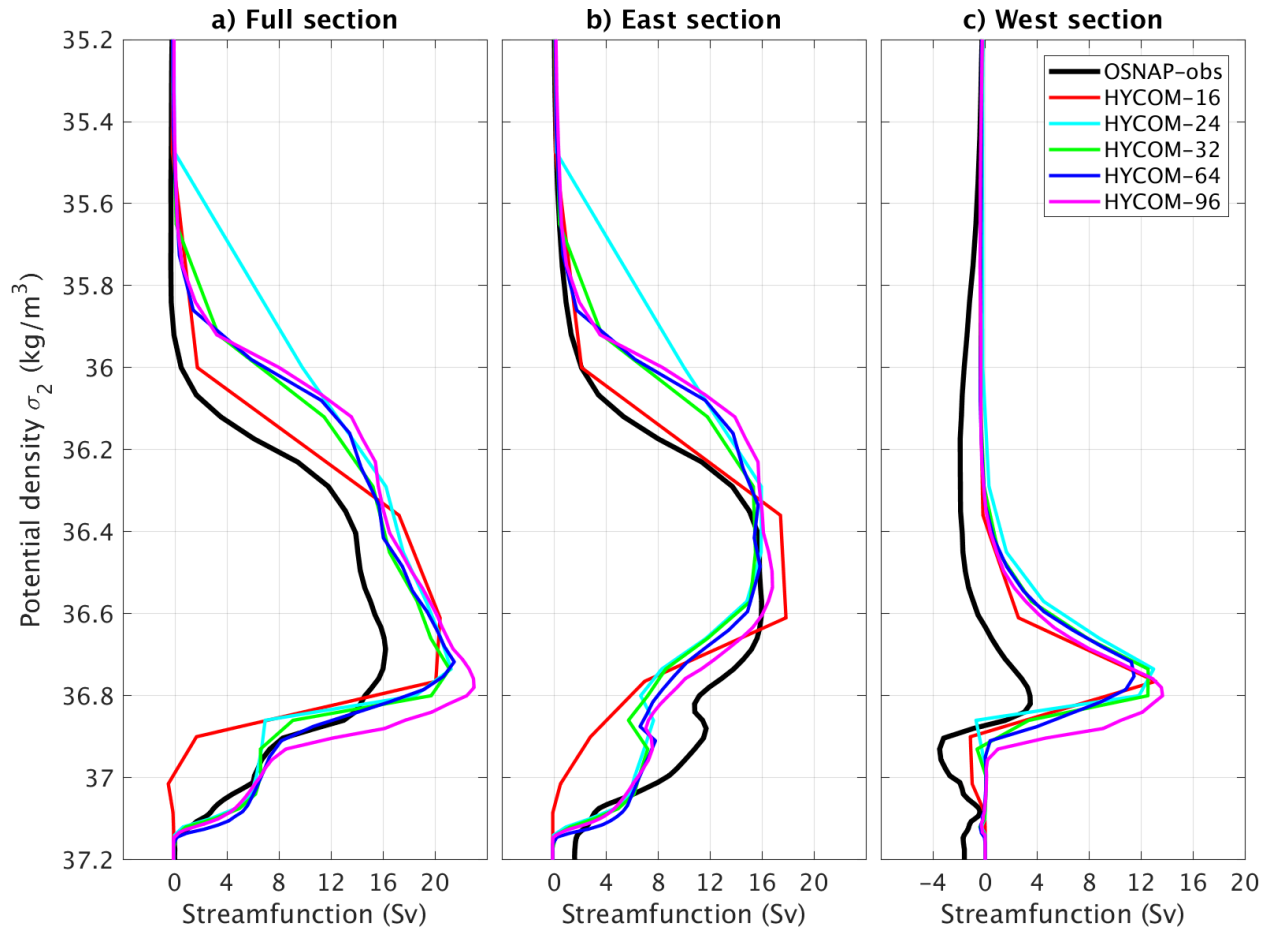
468  
 469 **Figure 15.** Modeled time mean meridional overturning streamfunction (in Sv) as a function of  
 470 density ( $\sigma_2$ ,  $\text{kg/m}^3$ ) and latitude in five  $1/12^\circ$  Atlantic HYCOM simulations with different vertical  
 471 resolutions: a) 16, b) 24, c) 32, d) 64, and e) 96 layers, respectively. The results show that expect  
 472 the 16-layer simulation, the other four simulations have an overall similar overturning  
 473 streamfunction structure.



474

475 **Figure 16.** Difference in modeled time-mean meridional overturning streamfunction (in Sv) as a  
 476 function of density and latitude in four 1/12 Atlantic HYCOM simulations with a) 16, b) 24, c) 32,  
 477 and d) 64 layers, respectively, compared to the 96-layer simulation as a reference. Blue color  
 478 indicates streamfunction value is lower in the low-resolution simulation and vice versa. The gray  
 479 and black contours are with 1 and 2 Sv interval, respectively.





480

481 **Figure 17.** Time mean meridional overturning streamfunction (in Sv) across the OSNAP sections  
 482 from the observations and five  $1/12^\circ$  Atlantic HYCOM simulations with different vertical  
 483 resolutions from 16 to 96 layers. The results are presented for a) full section (Labrador-Greenland-  
 484 Scotland), b) East section (Greenland-Scotland), and west section (Labrador-Greenland).

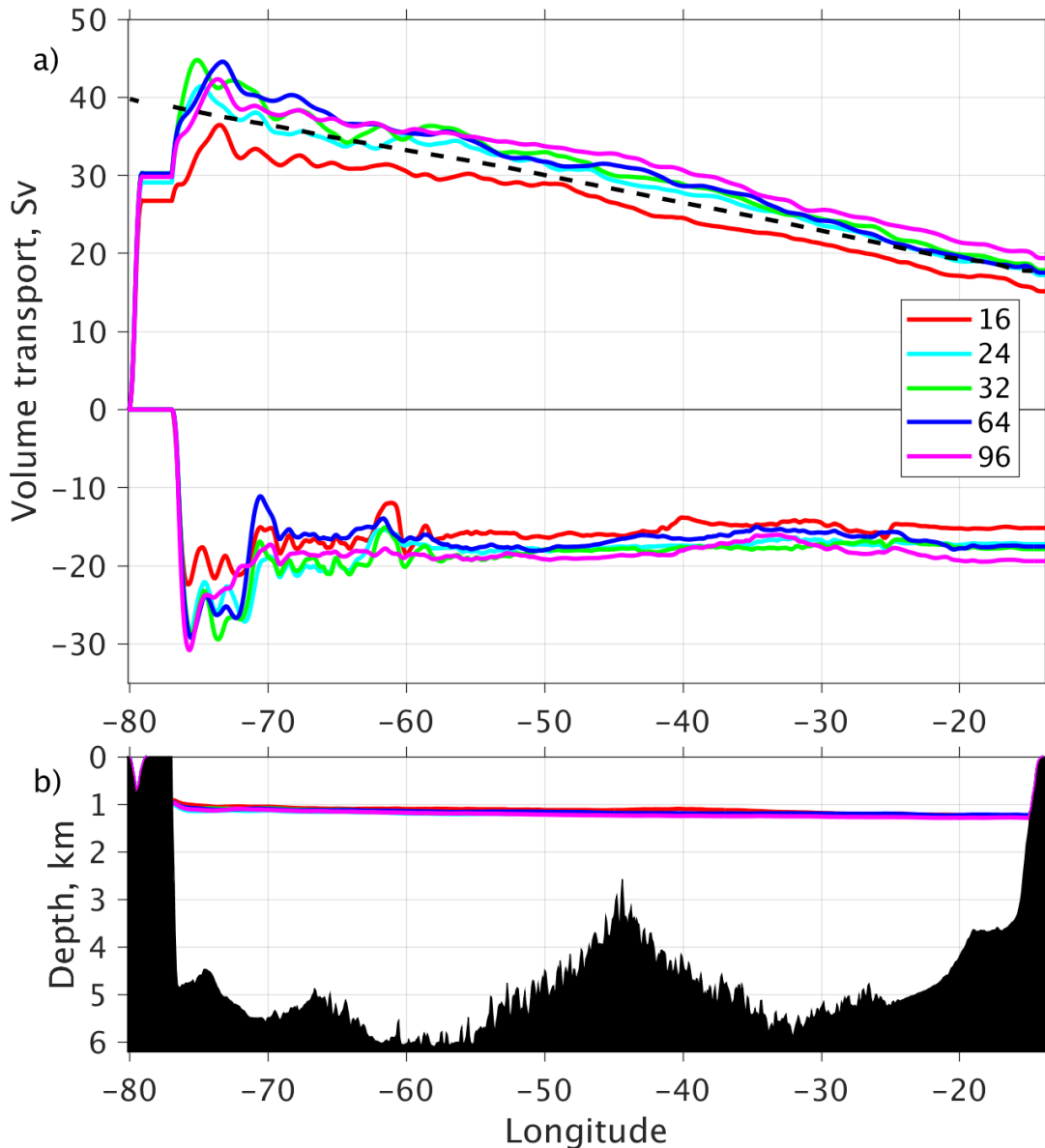
### 485 3.3 Horizontal Structure of the Subtropical and Subpolar North Atlantic Circulation

486 The AMOC, as discussed in previous section, provides a zonally integrated view of the basin-  
 487 wide circulation in the North Atlantic. For a comprehensive view, one should also examine the  
 488 horizontal structure of the circulation. Figure 18 displays the modeled cumulative transport (from  
 489 west to east) along the RAPID line near  $26^\circ\text{N}$  for the upper and lower limb of the AMOC, separated  
 490 by density ( $\sigma_2$ ) interface of  $36.52 \text{ kg/m}^3$  which is located at approximately 1000 m and slightly  
 491 shallower on the western side (Figure 18b). Above this interface, one can see the signature of the  
 492 northward western boundary current transports in the Florida Strait and east of Abaco (i.e., the

493 Florida Current and Antilles Current, respectively), and the broad southward transport over the  
494 Atlantic basin east of about 70°W. The latter is comparable to the Sverdrup transport that is  
495 calculated from the wind stress curl (dashed black line in Figure 18a). This is not surprising as the  
496 interior flow of the subtropical North Atlantic gyre is, to a good approximation, in Sverdrup  
497 balance (Wunsch and Roemmich, 1985; Schmitz et al., 1992; Wunsch, 2011). In the lower limb,  
498 the modeled circulation pattern across this latitude consists of a southward DWBC and some  
499 recirculation west of 70°W. East of 70°W in the ocean interior, the cumulative time-mean transport  
500 is relatively flat (Figure 18a), indicating that there is no significant meridional mean flow across  
501 this latitude in the model. Overall, all five experiments exhibit a similar transport pattern (Figure  
502 18), except again for the 16-layer case. Thus, the vertical resolution does not play a significant role  
503 in defining the horizontal structure of the meridional transports in the subtropical North Atlantic  
504 for 32+ layers.

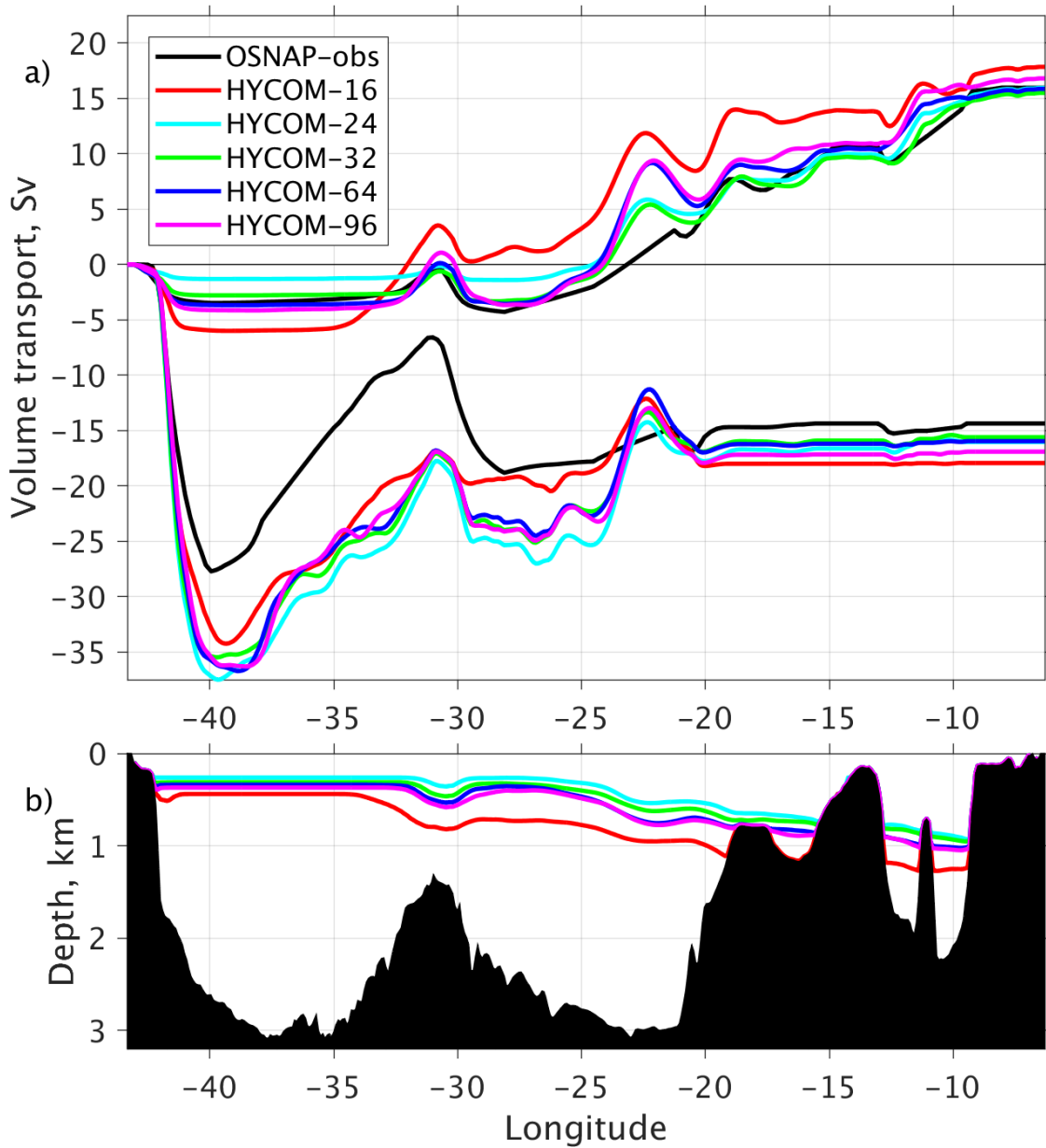
505 A similar plot can be performed further north for the subpolar region. Figure 19 displays the  
506 eastward cumulation of the meridional transport in the upper and lower limbs of the AMOC across  
507 the northern North Atlantic along the east OSNAP section from Greenland to Scotland near 59°N.  
508 The upper and lower limbs are separated by the density surface  $\sigma_2 = 36.6 \text{ kg/m}^3$  (equivalent to  $\sigma_\theta$   
509 of  $27.50 \text{ kg/m}^3$ ) as shown in Figure 19b. In the upper limb, both the magnitude and structure of  
510 the modeled transport are comparable to the observations. In the lower limb, the transport structure  
511 agrees, but the magnitude of the modeled transport is significantly higher than in the OSNAP  
512 observations. The largest difference is found in the Irminger Basin. The modeled full water column  
513 western boundary current transport is about 40 Sv (Figure 20), compared to 31.2 Sv in OSNAP  
514 observations during 2014-2018. The historical observations of the western boundary current at this  
515 location have yielded a similar volume transport of 32.1 Sv (Sarafanov et al., 2012) and 33.1 Sv

516 (Daniault et al., 2016), from 7 annual surveys in 2002-2008 and 6 biannual surveys in 2002-2012,  
 517 respectively. The higher model transport is associated with a stronger gyre recirculation in the  
 518 LSW layer. As in the subtropics, the horizontal circulation does not differ much with 32 or more  
 519 layers.



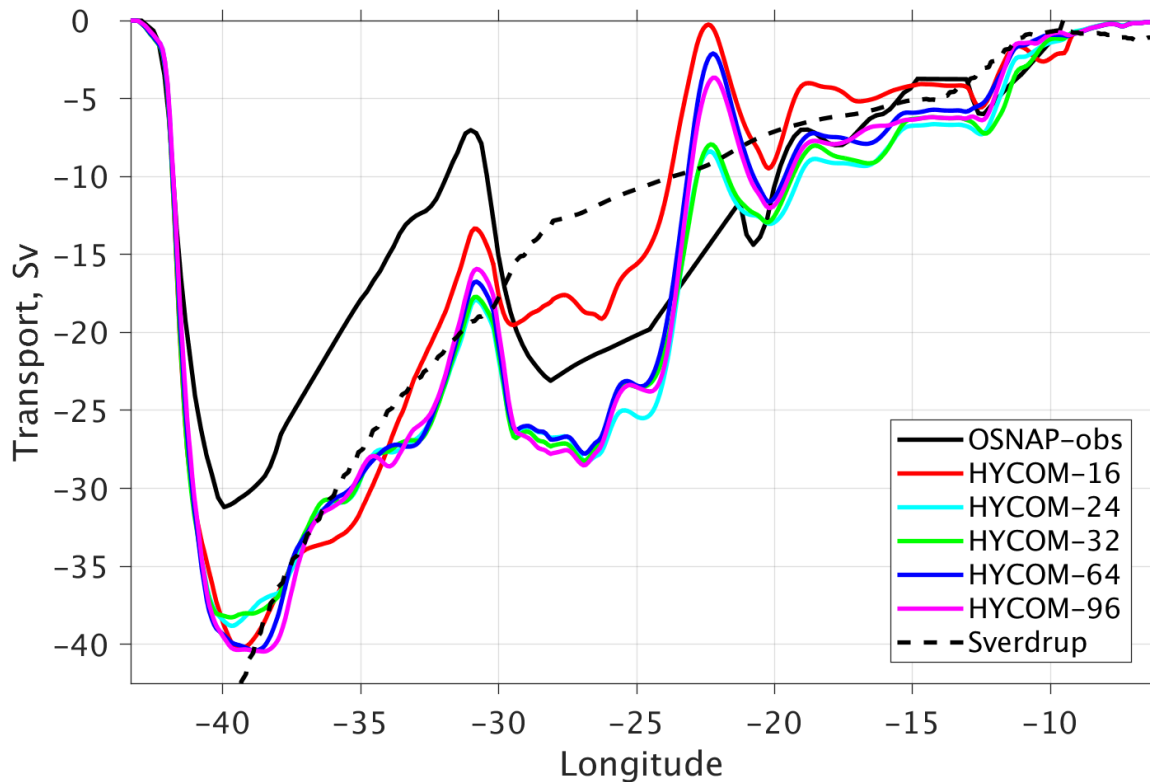
520  
 521 **Figure 18.** Horizontal structure of the subtropical circulation along the RAPID line near 26°N. a)  
 522 Time-mean (eastward) cumulative volume transport (in Sv) in the upper and lower limbs of the  
 523 Atlantic meridional overturning circulation (AMOC) from five 1/12° HYCOM simulations, with  
 524 vertical resolution of 16, 24, 32, 64, and 96 layers, respectively. The black dash line indicates the  
 525 Sverdrup transport calculated from wind-stress curl, integrated westward and multiplied by -1 to  
 526 be comparable with the eastward cumulative upper limb transports; b) bathymetry along the

527 RAPID line and the interface of density surface that separates the upper (northward) and lower  
 528 (southward) limb of the AMOC.



529

530 **Figure 19.** Horizontal structure of the subpolar circulation along the east OSNAP section from Greenland  
 531 to Scotland (see Figure A1 for location). a) Time-mean (eastward) cumulative volume transport (in Sv) in  
 532 the upper and lower limbs of the Atlantic meridional overturning circulation (AMOC) from five  $1/12^\circ$   
 533 HYCOM simulations, with vertical resolution of 16, 24, 32, 64, and 96 layers, respectively; black line  
 534 denote the observational estimate from b) bathymetry along the RAPID line and the interface of density  
 535 surface of  $27.50 \text{ kg/m}^3$  that separates the upper (northward) and lower (southward) limb of the AMOC.



536  
 537 **Figure 20.** Cumulative (eastward) full water column transport along the east ONSAP section. Solid black  
 538 line is estimated from OSNAP observations; colored lines are the model transports from five 1/12°  
 539 HYCOM simulations, with vertical resolution of 16, 24, 32, 64, and 96 layers, respectively; black  
 540 dashed line are the Sverdrup transport calculated from wind stress curl.

541 East of about 39°W across the east ONSAP section, the modeled full water column meridional  
 542 flow is generally northward, including contributions of both the subpolar gyre and the AMOC  
 543 components. Interestingly, the pattern of the modeled full water column transport between 39°W  
 544 and eastern boundary is comparable to that of the Sverdrup transport (Figure 20 dashed line), even  
 545 though the agreement is not as good as in the subtropics. The deviations are found in the 30-20°W  
 546 range where the subpolar gyre recirculates around the Iceland Basin, including a standing eddy  
 547 centered near 22°W in the deepest portion of the Iceland Basin (Figure 20b). The agreement  
 548 between the modeled transport and the Sverdrup transport is surprising because a) the Sverdrup  
 549 balance is not deemed to hold at this latitude where it takes multiple decades to achieve dynamical  
 550 equilibrium (Wunsch, 2011) and b) the AMOC is deemed as driven by basin-scale density  
 551 difference, not by the wind within the subpolar North Atlantic. The results in Figure 20 suggest

552 that much of the modeled subpolar circulation is driven by the large-scale wind, although the water  
553 masses undergo buoyancy loss and become denser as they flow around the northern rim of the  
554 subpolar North Atlantic. Regarding to model sensitivity, other than a weaker recirculation in the  
555 Iceland Basin in the 16-layer simulation, all five simulations exhibit similar zonal structure of the  
556 full-water column transport across this section. Thus, except for the 16-layer configuration, the  
557 vertical resolution does not play a significant role in the horizontal structure of the barotropic  
558 transports in the subpolar North Atlantic.

#### 559 **4. Summary and Discussion**

560 As pointed out in Stewart et al. (2017), few studies have documented the impact of the vertical  
561 resolution on OGCMs and there is no consensus on how one should construct the vertical grid to  
562 represent the vertical structure of the baroclinic modes as well as the distribution of distinct water  
563 masses throughout the global ocean. Stewart et al. (2017) proposed that the purpose of a vertical  
564 grid is primarily to resolve the vertical structure of the horizontal flow and that the vertical grids  
565 should be constructed based on their ability to represent baroclinic modal structure. Although not  
566 emphasized in Stewart et al. (2017), another fundamental purpose of the vertical grids in OGCMs  
567 is to represent accurately the distinct water masses that originate in different part of the ocean and  
568 occupy/circulate in different depth and/or density range of the water column. This study examines  
569 the impact of vertical resolution on a) the baroclinic modes and b) water mass representation and  
570 the large-scale circulation in the Atlantic. We find that both the 50 well-positioned  $z$  levels of  
571 Stewart et al. (2017) and the standard 32-layer HYCOM configuration are adequate to represent  
572 the zero-crossing depths of the first five baroclinic modes in mid-latitudes. The current OGCMs  
573 horizontal resolution resolves at most the first five Rossby radii of deformation and the vertical  
574 resolution currently used in OGCMs is therefore adequate in representing the corresponding

575 vertical structure of the first five modes. The most commonly used OGCM vertical grids also  
576 satisfy the vertical grid requirement of Stewart et al. (2017) for the first two modes, but there is  
577 definitely an advantage in using density layers instead of levels in representing higher modes. A  
578 100-level geopotential configuration cannot satisfy fully Stewart et al. (2017)'s grid requirement  
579 for the first five modes while a 96-layer isopycnic configuration does. This is primarily because a  
580 minimum of three levels is required in  $z$ -coordinate model to represent a single water mass versus  
581 only one constant density layer in isopycnic coordinate models, thus giving a factor of three  
582 advantage to the latter.

583 Vertical resolution significantly impacts the representation of deep water masses and hence the  
584 structure of the Atlantic meridional overturning circulation (AMOC). A coarse vertical resolution  
585 (16 layers) simulation exhibits virtually no transport in the dense overflow water which leads to a  
586 weaker and significantly shallower AMOC despite resolving the first baroclinic mode throughout  
587 the domain, whereas there are overall very small differences in the subtropical and subpolar North  
588 Atlantic circulation in the simulations with finer vertical resolution (24 to 96 layers). As the vertical  
589 resolution is increased from 24 to 96 layers, there is a slight increase in the magnitude of the  
590 AMOC and a slight deepening of the southward-flowing North Atlantic Deep Water that leads to  
591 a better agreement with the observations.

592 With increased vertical resolution, the OGCMs better resolve both the vertical modes and the  
593 water masses, but their relative importance differs. With 16 layers, the vertical resolution can  
594 represent the first baroclinic Rossby radius and the vertical structure of the first baroclinic mode  
595 to a good approximation. It however cannot represent the dense overflow water which leads to a  
596 rather unrealistic structure of the AMOC. The lower SSH variability seen in the 16-layer  
597 configuration primarily viewed as a consequence of not resolving higher baroclinic modes, but the

598 weaker AMOC may also lead to a weaker and less unstable northward-flowing Gulf Stream and  
599 North Atlantic Current.

600 In conclusion, we argue that accurately representing the water mass is more important than  
601 representing the vertical modes in simulating the basin-scale circulation and mesoscale variability  
602 and should be considered first when constructing a vertical grid. This does not mean that the  
603 vertical modes are not important and, with higher horizontal resolution that now starts to resolve  
604 sub-mesoscale eddies, one could see more sensitivity to vertical resolution, especially at higher  
605 frequencies and in the presence of internal tides (Xu et al., 2022). High vertical resolution is  
606 expected to be beneficial in the representation of the stratification associated with the pycnocline,  
607 hence the generation of internal tides. Also, in this study we have focused on whether or to what  
608 extent the vertical resolution impacts the basin-scale aspects of the North Atlantic circulation (i.e.,  
609 AMOC and subpolar/subtropical gyres). Vertical resolution can also impact regional processes,  
610 such as upwelling and associated diapycnal mixing. The impact on these detailed processes needs  
611 to be further examined in future studies.

## 612 **Data Availability Statement**

613 The Mean Dynamic topography (MDT) are available in AVISO (<https://aviso.altimetry.fr>); the  
614 gridded Sea Surface Height (SSH) are distributed through Copernicus Marine Service  
615 (<https://marine.copernicus.eu>); the RAPID observations are available at <https://rapid.ac.uk>; and the  
616 OSNAP observations are available at <https://o-snap.org>. The full-resolution model outputs are  
617 stored in the U.S. Army Engineer Research and Development Center (ERDC) and U.S. Navy DoD  
618 Supercomputing Resource Center (DSRC) archive server. The key model results represented in  
619 this study are available in the data repository (<http://doi.org/10.5281/zenodo.7751007>). The script  
620 to run the numerical simulations and to plot the figures presented in the paper are available by  
621 request.



622 **Acknowledgement**

623 XX, EPC, and AJW acknowledge support from the Office of Naval Research (ONR) grants  
624 N00014-19-1-2717 and N00014-20-1-2769, the National Science Foundation (NSF) grants OCE-  
625 2038449, and the National Aeronautics and Space Administration (NASA) grants  
626 80NSSC20K1135 and 80NSSC21K1500. The high-resolution HYCOM simulations were  
627 performed on supercomputers at the U.S. Army Engineer Research and Development Center  
628 (ERDC) in Vicksburg, Mississippi, and the U.S. Navy DoD Supercomputing Resource Center  
629 (DSRC) in Stennis Space Center, Mississippi, using computer time provided by the U.S. DoD  
630 High Performance Computing Modernization Program. The authors also thank Dr. Stewart and  
631 the anonymous reviewer for their constructive comments, which improves this paper significantly.

632 **APPENDIX**

633 **a) Depth and layer distribution of the first 9 baroclinic modes**

634 The zero-crossing interfaces of baroclinic mode divide the water column in layers. For example,  
 635 the first baroclinic mode has one zero-crossing interface which divides the water column into two  
 636 layers, the second baroclinic mode has two zero-crossing interfaces that divide the water column  
 637 into three layers, etc. Table A1 lists the spatially averaged depth of the zero-crossing interfaces  
 638 associated with the baroclinic modes 1, 2, 3, 5, 7, and 9. These z levels can be used to construct  
 639 the low-resolution configuration to represent the Rossby radius (and/or vertical modes) in z-level  
 640 coordinate (Figures 2a-c, 3a-c). Table A2 lists the spatially averaged densities of the layers that  
 641 are divided by these zero-crossing interfaces and can be used to construct the low-resolution  
 642 configuration to represent the Rossby radius (and/or vertical modes) in isopycnic coordinate  
 643 (Figures 2d-f, 3d-f).

644 **Table A1.** Spatially averaged depth (in meter) of the zero-crossing interfaces of the baroclinic  
 645 modes 1, 2, 3, 5, 7, and 9 in the North and Equatorial Atlantic Ocean as calculated from ocean  
 646 climatology GDEM.  
 647

Interface index	$m=1$	$m=2$	$m=3$	$m=5$	$m=7$	$m=9$
1	1170	286	132	63	48	41
2		1787	694	292	172	124
3			2136	693	397	272
4				1271	691	466
5				2557	1068	698
6					1620	979
7					2779	1329
8						1876
9						2915

648

649

650 **Table A2.** Spatially averaged densities ( $\sigma_2$  in  $\text{kg/m}^3$ ) of the layers divided by the zero-crossing  
 651 interface of the baroclinic modes 1, 2, 3, 5, and 9 in the North and Equatorial Atlantic Ocean as  
 652 calculated from ocean climatology GDEM.  
 653

Layer index	$m=1$	$m=2$	$m=3$	$m=5$	$m=7$	$m=9$
1	35.80	34.45	33.80	33.46	33.37	33.33
2	36.96	36.42	35.65	34.91	34.42	34.12
3		37.01	36.71	35.88	35.41	35.08
4			37.03	36.50	35.98	35.63
5				36.90	36.41	36.05
6				37.04	36.73	36.37
7					36.95	36.63
8					37.05	36.83
9						36.98
10						37.05

654 **b) North and Equatorial Atlantic HYCOM configuration**

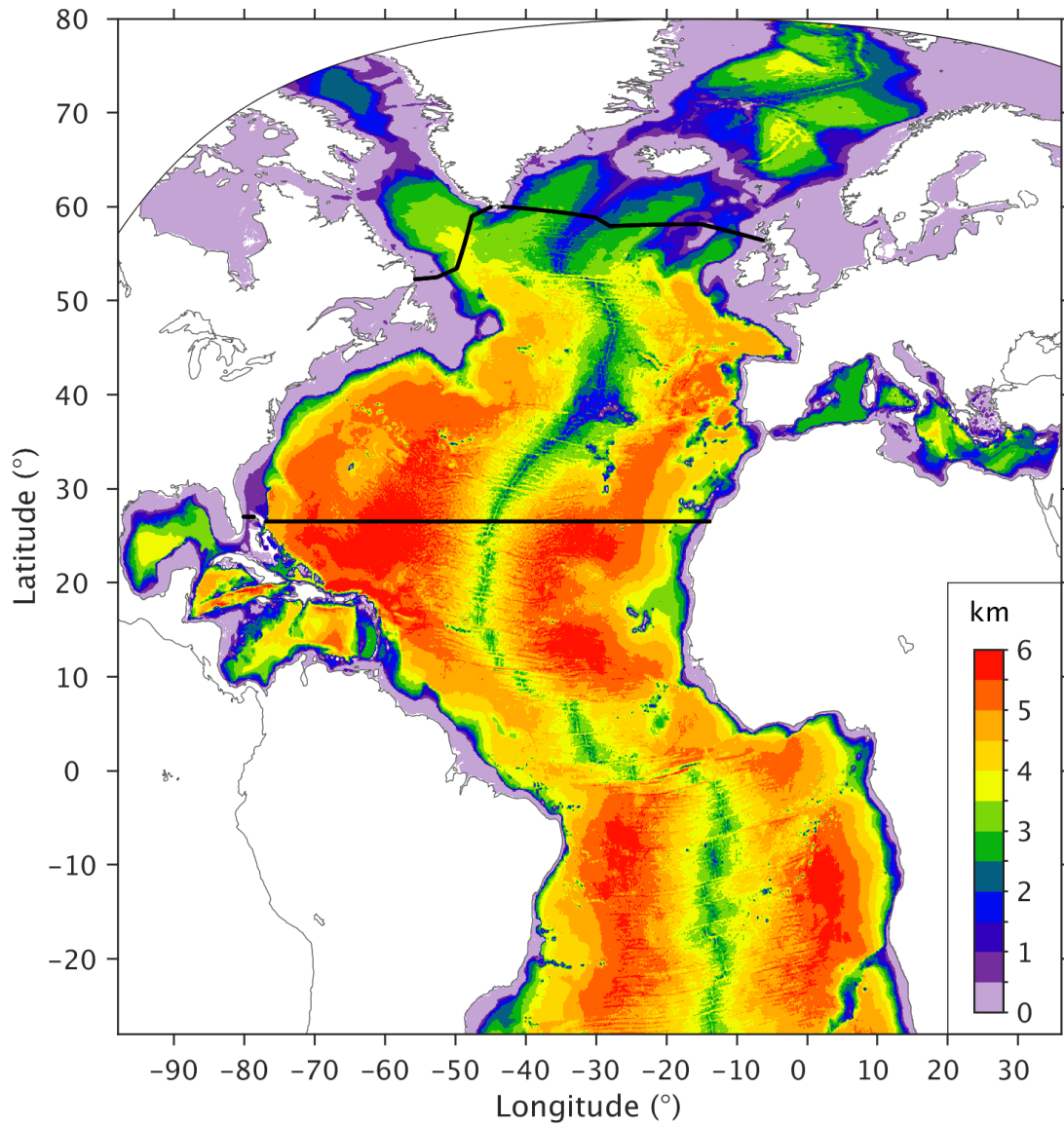
655 The North and Equatorial Atlantic HYCOM computational domain extends from 28°S to the  
 656 Fram Strait at 80°N (Figure A1). The northern and southern boundaries are “vertical wall” with  
 657 no normal flows, and within a buffer zone of 3° to these two boundaries, the model temperature  
 658 and salinity are restored to monthly ocean climatology (Carnes 2009) with an *e*-folding time of 5-  
 659 60 days, which increases with distance from the boundary. The atmospheric forcing combines the  
 660 climatological monthly means from the 40-year European Center for Medium Range Weather  
 661 Forecasts Reanalysis (ERA040, Uppala et al. 2005) and high-frequency (6-hourly) wind anomalies  
 662 from the Fleet Numerical Meteorology and Oceanography Center’s Navy Operational Global  
 663 Atmospheric Prediction System (NOGAPS, Rosmond et al. 2002). The reason for the latter is that  
 664 ocean convection is strongly influenced by synoptic weather systems and high-frequency winds  
 665 are important for proper representation of the surface mixed layer physics (Kantha and Clayson,  
 666 1994; Large et al. 1994). Wind anomalies for year 2003, a year with neutral North Atlantic  
 667 Oscillation is used for this purpose. The surface heat flux includes the shortwave and longwave  
 668 radiations that are directly from ERA-40, and the latent and sensible heat fluxes that are calculated

669 using the model sea surface temperature (SST) and bulk formulas of Kara et al. (2005). The surface  
670 freshwater flux includes evaporation, precipitation, and river runoffs. The model sea surface  
671 salinity is also restored toward the monthly climatology with a relatively strong restoring strength  
672 of 15 m per 30 days.

673 Five simulations are considered in this study, all with an eddying horizontal resolution of  $1/12^\circ$   
674 and a vertical resolution of 16, 24, 32, 64, and 96 layers, respectively. The 32-layer configuration  
675 was the standard of the Atlantic simulation (Xu et al., 2010; 2012), from which the resolution is  
676 doubled and tripled in the 64 and 96-layer configurations (by inserting one and two model layers  
677 between each two layers) and cut in half in the 16-layer configuration (combining two layers into  
678 one). The 24-layer configuration was designed to investigate the impact of reducing resolution in  
679 the upper water column (the top 8 model layers are the same as in the 16-layer configuration and  
680 the lower 16 layers are the same as the standard 32-layer configuration).

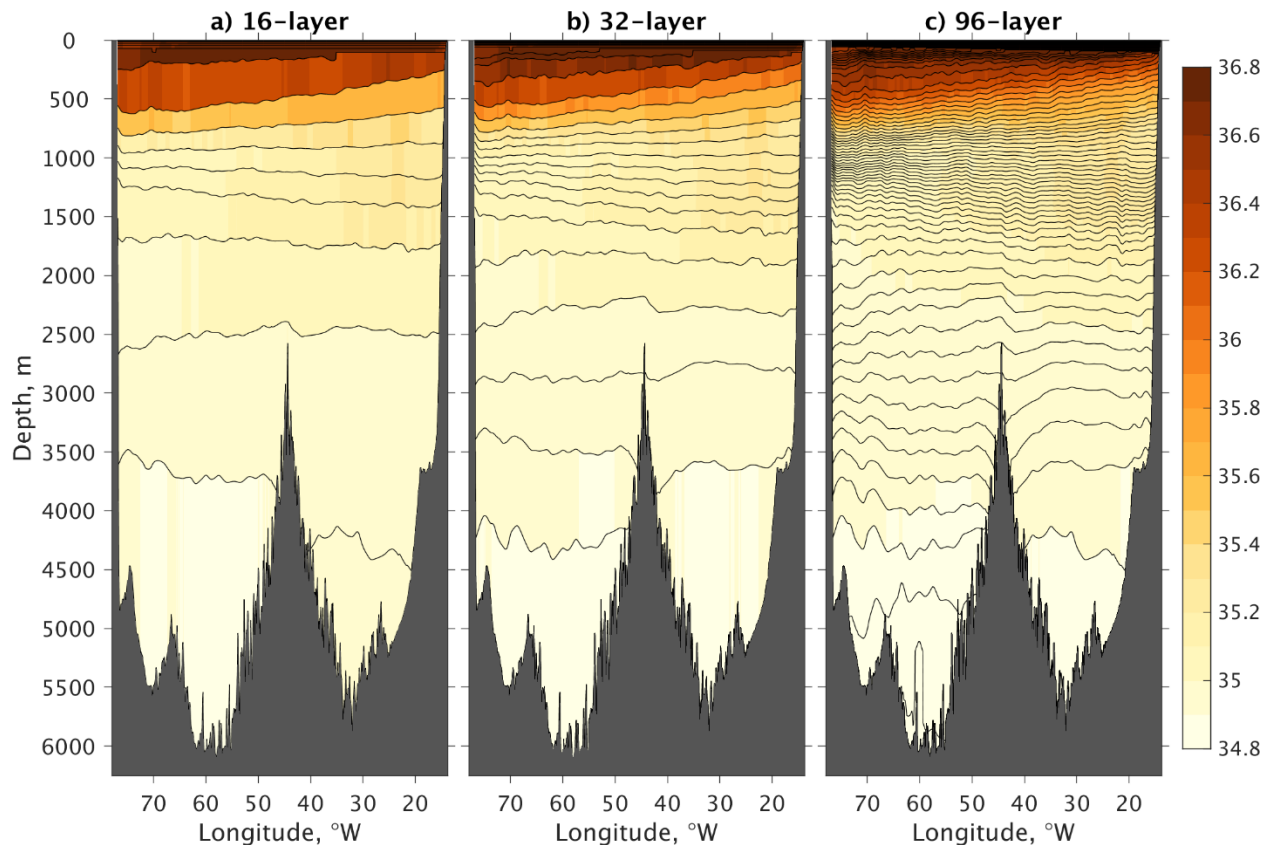
681 All five simulations are initialized with January temperature and salinity from ocean  
682 climatology (Carnes 2009) and run for 20 years. Figure A2 displays a vertical view of the model  
683 layers in the initialization along the RAPID section near  $26^\circ\text{N}$ , for 16, 32, and 96-layer  
684 configurations, from which one can see that the resolution below about 1500 m is quite coarse in  
685 the 16-layer set up. We focus on the last five years of the integration, which is deemed to be  
686 representative of the circulation after spin-up, i.e., the simulation reaches statistical equilibrium in  
687 terms of kinetic energy and volume transports, although the modeled temperature and salinity are  
688 expected to continue to adjust over much longer time scales.

689



690

691 **Figure A1.** Bathymetry (in km) of the North and equatorial Atlantic domain used in the HYCOM  
 692 simulations with different vertical resolutions. Black lines near 26°N and across the subpolar  
 693 region denote the location of the RAPID (e.g., Smeed et al., 2018) and the OSNAP (e.g., Loizer et  
 694 al., 2019) observations, to which the modeled transport structure is examined in detail.



695

696 **Figure A2.** Model initial salinity along with the model layer interfaces across the Atlantic along  
 697 the RAPID line in three  $1/12^\circ$  HYCOM simulations with different 16, 32, and 96 layers,  
 698 respectively.

699 **REFERENCE**

700 Adamec, D., 1988. Numerical simulations of the effects of seamounts and vertical resolution on  
 701 strong ocean flows. *J. Phys. Oceanogr.* 18, 258–269.

702 Barnier, B., Hua, B.L., Provost, C.L., 1991. On the catalytic role of high baroclinic modes in eddy-  
 703 driven large-scale circulations. *J. Phys. Oceanogr.* 21, 976–997.

704 Bleck, R., 2002. An oceanic general circulation model framed in hybrid isopycnic-Cartesian  
 705 coordinates. *Ocean Model.* 4, 55–88,.

706 Bryan, K., 1969. A numerical method for the study of the circulation of the world ocean. *J. Comput.*  
 707 *Phys.* 4, 347-376.

708 Carnes, M. R., 2009. Description and evaluation of GDEM-V3.0. Naval Research Laboratory  
 709 Memo. Rep. NRL/MR/7330–09-9165, 21 pp. [Available online at  
 710 <http://www7320.nrlssc.navy.mil/pubs/2009/carnes-2009.pdf>.]

711 Chassignet, E. P., Smith, L. T., Halliwell, G. R., Bleck, R., 2003. North Atlantic simulations with  
 712 the hybrid coordinate ocean model (HYCOM): Impact of the vertical coordinate choice,  
 713 reference pressure, and thermobaricity. *J. Phys. Oceanogr.* 33, 2504–2526.

714 Chassignet, E.P., Hurlburt, H.E., Smedstad, O.M., Halliwell, G.R., Wallcraft, A.J., Metzger, E.J.,  
715 Blanton, B.O., Lozano, C., Rao, D.B., Hogan, P.J., Srinivasan, A., 2006. Generalized vertical  
716 coordinates for eddy-resolving global and coastal ocean forecasts. *Oceanogr.* 19, 20-31.

717 Chassignet, E.P., Yeager, S.G., Fox-Kemper, B., Bozec, A., Castruccio, F., Danabasoglu, G.,  
718 Horvat, C., Kim, W.M., Koldunov, N., Li, Y., Lin, P., Liu, H., Sein, D., Sidorenko, D., Wang,  
719 Q., Xu, X., 2020. Impact of horizontal resolution on global ocean-sea-ice model simulations  
720 based on the experimental protocols of the Ocean Model Intercomparison Project phase 2  
721 (OMIP-2). *Geosci. Model Dev.* 13, 4595-4637.

722 Chassignet, E. P., Xu, X., 2017. Impact of horizontal resolution ( $1/12^\circ$  to  $1/50^\circ$ ) on Gulf Stream  
723 separation, penetration, and variability. *J. Phys. Oceanogr.*, 47, 1999–2021.

724 Chassignet, E.P., Xu, X., 2021. On the importance of high-resolution in large scale ocean models.  
725 *Adv. Atmos. Sci.*, 38, 1621-1634.

726 Chassignet, E. P., Xu, X., Bozec, A., Uchida, T., 2023. Impact of the New England seamount chain  
727 on Gulf Stream pathway and variability. *J. Phys. Oceanogr.* in press.

728 Daniault, N., Mercier, H., Lherminier, P., Sarafanov, A., Falina, A., Zunino, P., Pérez, F.F., Ríos,  
729 A.F., Ferron, B., Huck, T. and Thierry, V., 2016. The northern North Atlantic Ocean mean  
730 circulation in the early 21st century. *Prog. in Oceanogr.* 146, 142-158.

731 Frajka-Williams, E., Ansrorge, I. J., Baehr, J., Bryden, H. L., Chidichimo, M. P., Cunningham, S.  
732 A., Danabasoglu, G., Dong, S., Donohue, K. A., Elipot, S., 2019. Atlantic meridional  
733 overturning circulation: Observed transport and variability. *Front. Mar. Sci.* 6, 260.

734 Hallberg, R., 2013. Using a resolution function to regulate parameterizations of oceanic mesoscale  
735 eddy effects. *Ocean Model.* 72, 92–103.

736 Hirschi, J. J.-M., Barnier, B., Böning, C., Biastoch, A., Blaker, A. T., Coward, A., Danilov, S.,  
737 Drijfhout, S., Getzlaff, K., Griffies, S. M., Hasumi, H., Hewitt, H., Iovino, D., Kawasaki, T.,  
738 Kiss, A. E., Koldunov, N., Marzocchi, A., Mecking, J. V., Moat, B., Molines, J.-M., Myers,  
739 P. G., Penduff, T., Roberts, M., Treguier, A.-M., Sein, D. V., Sidorenko, D., Small, J., Spence,  
740 P., Thompson, L., Weijer, W., Xu, X., 2020. The Atlantic meridional overturning circulation  
741 in high-resolution models. *J. Geophys. Res.-Oceans.* 125, e2019JC015522.

742 Hurlburt, H. E., Hogan, P. J., 2000. Impact of  $1/8^\circ$  to  $1/64^\circ$  resolution on Gulf Stream model–data  
743 comparisons in basin-scale subtropical Atlantic Ocean models. *Dyn. Atmos. Oceans.* 32, 283–  
744 329.

745 Kantha, L. H., Clayson, C. A., 1994. An improved mixed layer model for geophysical applications.  
746 *J. Geophys. Res.-Oceans.* 99, 25 235–25 266.

747 Kara, A. B., Hurlburt, H. E., Wallcraft, A. J., 2005. Stability dependent exchange coefficients for  
748 air–sea fluxes. *J. Atmos. Oceanic Technol.* 22, 1080–1094.

749 Klein, P., Lapeyre, G., Siegelman, L., Qiu, B., Fu, L.-L., Torres, H., Su, Z., Menemenlis, D., Le  
750 Gentil, S., 2019. Ocean-scale interactions from space. *Earth and Space Science*, 6, 795–817.

751 Large, W. G., McWilliams, J. C., Doney, S. C., 1994. Ocean vertical mixing: A review and a model  
752 with a nonlocal boundary layer parameterization. *Rev. Geophys.* 32, 363–403.

- 753 Legg, S., Chang, Y., Chassignet, E.P., Danabasoglu, G., Ezer, T., Gordon, A.L., Griffes, S.,  
754 Hallberg, R., Jackson, L., Large, W., Özgökmen, T., Peters, H., Price, J., Riemenschneider,  
755 U., Wu, W., Xu, X., Yang, J., 2009. Improving oceanic overflow representation in climate  
756 models: the Gravity Current Entrainment Climate Process Team. *Bull. Amer. Met. Soc.* 90,  
757 657-670.
- 758 Le Sommer, J., Chassignet, E.P., Wallcraft, A.J., 2018. Ocean circulation modeling for operational  
759 oceanography: Current status and future challenges. In "New Frontiers in Operational  
760 Oceanography", Chassignet, E., Pascual, A., Tintoré, J., Verron J. (Eds.), GODAE  
761 OceanView, 289-306.
- 762 Lévy, M., Klein, P., Tréguier, A.-M., Iovino, D., Madec, G., Masson, S., Takahashi, K., 2010.  
763 Modifications of gyre circulation by sub-mesoscale physics. *Ocean Model.* 34, 1–15.
- 764 Lozier, M.S., Li, F., Bacon, S., Bahr, F., Bower, A.S., Cunningham, S.A., de Jong, M.F., de Steur,  
765 L., deYoung, B., Fischer, J., Gary, S.F., 2019. A sea change in our view of overturning in the  
766 subpolar North Atlantic. *Sci.* 363(6426), 516-521.
- 767 McWilliams, J. C., 1996. Modeling the oceanic general circulation. *Annu. Rev. Fluid Mech.* 28,  
768 215–248.
- 769 Mulet, S., Rio, M.-H., Etienne, H., Artana, C., Cancet, M., Dibarboure, G., Feng, H., Husson, R.,  
770 Picot, N., Provost, C., and Strub, P. T., 2021. The new CNES-CLS18 global mean dynamic  
771 topography, *Ocean Sci.* 17, 789–808.
- 772 Paiva, A.M., Hargrove, J.T., Chassignet, E.P., Bleck, R., 1999. Turbulent behavior of a fine mesh  
773 (1/12 degree) numerical simulation of the North Atlantic. *J. Mar. Sys.* 21, 307-320.
- 774 Richardson, P. L., 1983. Eddy kinetic energy in the North Atlantic from surface drifters. *J.*  
775 *Geophys. Res.* 88, 4355–436.
- 776 Roberts, M. J., Jackson, L. C., Roberts, C. D., Meccia, V., Docquier, D., Koenigk, T., Ortega, P.,  
777 Moreno-Chamarro, E., Bellucci, A., Coward, A., Drijfhout, S., Exarchou, E., Gutjahr, O.,  
778 Hewitt, H., Iovino, D., Lohmann, K., Schiemann, R., Seddon, J., Terray, L., Xu, X., Zhang,  
779 Q., Chang, P., Yeager, S. G., Castruccio, F. S., Zhang, S., Wu, L., 2020. Sensitivity of the  
780 Atlantic meridional overturning circulation to model resolution in CMIP6 HighResMIP  
781 simulations and implications for future changes. *J. Adv. Model. Earth Syst.* 12,  
782 e2019MS002014.
- 783 Rosmond, T., Teixeira, J., Peng, M., Hogan, T., Pauley, R., 2002. Navy Operational Global  
784 Atmospheric Prediction System (NOGAPS): Forcing for ocean models. *Oceanogr.* 15, 99–  
785 108.
- 786 Sarafanov A., Falina, A., Mercier, H., Sokov, A., Lherminier, P., Gourcuff, C., Gladyshev, S.,  
787 Gaillard, F., Danialt N., 2012. Mean full-depth summer circulation and transports at the  
788 northern periphery of the Atlantic Ocean in the 2000s. *J. Geophys. Res.-Oceans.* 117, C01014.
- 789 Schmitz, W. J., Thompson, J. D., Luyten, J. R., 1992. The Sverdrup circulation for the Atlantic  
790 along 24°N. *J. Geophys. Res.-Oceans.* 97, 7251–7256.
- 791 Smith, L.T., Chassignet, E.P., Bleck, R., 2000. The impact of lateral boundary conditions and  
792 horizontal resolution on North Atlantic water mass transformations and pathways in an  
793 isopycnic coordinate ocean model. *J. Phys. Oceanogr.* 30, 137-159.



794 Smeed, D.A., Josey, S.A., Beaulieu, C., Johns, W.E., Moat, B.I., Frajka-Williams, E., Rayner, D.,  
795 Meinen, C.S., Baringer, M.O., Bryden, H.L. and McCarthy, G.D., 2018. The North Atlantic  
796 Ocean is in a state of reduced overturning. *Geophys. Res. Lett.* 45, 1527-1533.

797 Soufflet, Y., Marchesiello, P., Lemarié, F., Jouanno, J., Capet, X., Debreu, L., Benshila, R., 2016.  
798 On effective resolution in ocean models. *Ocean Model.* 98, 36–50.

799 Stanley, G.J., 2019. Neutral surface topology. *Ocean Model.* 138, 88-106.

800 Stewart, K. D., Hogg, A. M., Griffies, S. M., Heerdegen, A. P., Ward, M. L., Spence, P., England,  
801 M. H., 2017. Vertical resolution of baroclinic modes in global ocean models. *Ocean Model.*  
802 113, 50–65.

803 Uppala, S. M., KÅllberg, P. W., Simmons, A. J., Andrae, U., Da Costa Bechtold, V., Fiorino, M.,  
804 Gibson, J. K., Haseler, J., Hernandez, A., Kelly, G. A., Li, X., Onogi, K., Saarinen, S., Sokka,  
805 N., Allan, R. P., Andersson, E., Arpe, K., Balmaseda, M. A., Beljaars, A. C. M., Van De Berg,  
806 L., Bidlot, J., Bormann, N., Caires, S., Chevallier, F., Dethof, A., Dragosavac, M., Fisher, M.,  
807 Fuentes, M., Hagemann, S., Hólm, E., Hoskins, B. J., Isaksen, L., Janssen, P. A. E. M., Jenne,  
808 R., McNally, A. P., Mahfouf, J.-F., Morcrette, J.-J., Rayner, N. A., Saunders, R. W., Simon,  
809 P., Sterl, A., Trenberth, K. E., Untch, A., Vasiljevic, D., Viterbo, P., Woollen, J., 2005. The  
810 ERA-40 Re-Analysis. *Quart. J. Roy. Meteor. Soc.* 131, 2961–3012.

811 Weaver, A.J., Sarachik, E.S., 1990. On the importance of vertical resolution in certain ocean  
812 general circulation models. *J. Phys. Oceanogr.* 20, 600–609.

813 Wunsch, C., 2011. The decadal mean ocean circulation and Sverdrup balance, *J. Mar. Res.* 69,  
814 417-434.

815 Wunsch, C., Roemmich, D., 1985. Is the North Atlantic in Sverdrup balance? *J. Phys. Oceanogr.*  
816 15, 1876–1880

817 Xu, X., Chassignet, E. P., Price, J. F., Özgökmen, T. M., Peters, H., 2007. A regional modeling  
818 study of the entraining Mediterranean outflow. *J. Geophys. Res.-Oceans.* 112, C12005.

819 Xu, X., Schmitz Jr., W. J., Hurlburt, H. E., Hogan, P. J., Chassignet, E. P., 2010. Transport of  
820 Nordic Seas overflow water into and within the Irminger Sea: An eddy-resolving simulation  
821 and observations. *J. Geophys. Res.-Oceans.* 115, C12048.

822 Xu, X., Schmitz Jr., W. J., Hurlburt, H. E., Hogan, P. J., 2012. Mean Atlantic meridional  
823 overturning circulation across 26.5°N from eddy-resolving simulations compared to  
824 observations. *J. Geophys. Res.-Oceans.* 117, C03042.

825 Xu, X., Chassignet, E. P., Wallcraft, A. J., Arbic, B. K., Buijsman, M. C., Solano, M., 2022. On  
826 the spatial variability of the mesoscale sea surface height wavenumber spectra in the Atlantic  
827 Ocean. *J. Geophys. Res.-Oceans.* 127, e2022JC018769.

828 Xu, X., Rhines, P.B., Chassignet, E.P., 2016. Temperature-salinity structure of the North Atlantic  
829 circulation and associated heat and freshwater transports. *J. Climate.* 29, 7723-7741.

830 Xu, X., Rhines, P.B., Chassignet, E.P., 2018. On mapping the diapycnal water mass transformation  
831 of the North Atlantic Ocean. *J. Phys. Oceanogr.* 48, 2233-2258.

832